





Turbulent dam-break waves of Newtonian and non-Newtonian fluids

Andrea Del Gaudio¹ , George Constantinescu² , Francesco De Paola¹,
Cristiana Di Cristo¹  and Andrea Vacca¹ 

¹Dipartimento di Ingegneria Civile, Edile e Ambientale, Università di Napoli 'Federico II', Naples 80125, Italy

²Department of Civil and Environmental Engineering and IIHR-Hydrosience and Engineering, University of Iowa, IA 52240, USA

Corresponding author: George Constantinescu, sconstan@engineering.uiowa.edu

(Received 27 February 2025; revised 16 June 2025; accepted 26 August 2025)

The paper uses three-dimensional large eddy simulation (LES) to investigate the structure and propagation of dam break waves of non-Newtonian fluids described by a power-law rheology. Simulations are also conducted for the limiting case of a dam-break wave of Newtonian fluid (water). Turbulent dam-break waves are found to have a two-layer structure and to generate velocity streaks beneath the region in which the flow is strongly turbulent and lobes at the front. The bottom part of the wave resembles a boundary layer and contains a log-law sublayer, while the streamwise velocity is close to constant inside the top layer. The value of the von Kármán constant is found to reach the standard value (i.e. $\kappa \approx 0.4$) associated with turbulent boundary layers of Newtonian fluids only inside the strongly turbulent region near the front of Newtonian dam-break waves. Much higher values of the slope of the log law are predicted for non-Newtonian dam-break waves (i.e. $\kappa \approx 0.28$) and in the regions of weak turbulence of Newtonian waves. LES shows that a power-law relationship can well describe the temporal evolution of the front position during the acceleration and deceleration phases, and that increasing the shear-thinning behaviour of the fluid increases the speed of the front. The numerical experiments are then used to investigate the predictive abilities of shallow water equation (SWE) models. The paper also proposes a novel one-dimensional (1-D) SWE model which accounts for the bottom friction by employing a friction coefficient regression valid for power-law fluids in the turbulent regime. An analytical approximate solution is provided by splitting the current into an outer region, where the flow is considered inviscid and friction is neglected, and an inner turbulent flow region, close to the wave front. The SWE numerical and analytical solutions using a turbulent friction factor are found to be in better agreement with LES compared with the agreement shown by an SWE numerical model using a

laminar friction coefficient. The paper shows that inclusion of turbulence effects in SWE models used to predict high-Reynolds-number Newtonian and non-Newtonian dam break flows results in more accurate predictions.

Key words: geophysical and geological flows, shallow water flows

1. Introduction

The slumping of a liquid (e.g. water) column into an ambient fluid (e.g. air) producing a wave flowing over a solid surface has been widely studied in the literature. When the ambient fluid is weightless and inviscid, the resulting flow is the well-known dam-break problem, which can be schematised by the instantaneous opening of a gate delimiting a reservoir containing the liquid. This configuration is useful to analyse the dynamics of many unsteady, gravity-driven flows encountered in various geophysical phenomena (Delannay *et al.* 2017). For example, the water wave may be caused by the collapse of a dam or of a levee, or by a tsunami. Moreover, dam-break-like waves occur in the presence of mud flows (Takahashi *et al.* 2014) and in the minerals industry, where tailings are transported from the mine to the disposal facilities (Haldenwang *et al.* 2006). The prediction of relevant hydraulic quantities associated with flood hazards and mud flows is very important for risk analysis.

Numerous experimental studies investigated the propagation of water dam-break waves over a fixed bottom. The main goal of these studies was to describe the wave dynamics in terms of the macro-scale properties of the flow, e.g. water level evolution and water wave propagation. A comprehensive review of these investigations is given by Aureli *et al.* (2023). Only a limited number of investigations tried to describe the turbulence characteristics close to the bottom wall. Fraccarollo & Toro (1995) performed point velocity measurements at some locations using a current meter, providing time series data of point velocity. Aleixo, Soares-Frazão & Zech (2011) measured the mean (two-dimensional; 2-D) velocity profiles in a dam-break flow, while Aleixo *et al.* (2014) measured the vertical distributions of the Reynolds stresses using particle tracking velocimetry. Owing to the limitations of the experimental technique, the mean velocity and Reynolds stress profiles were not resolved close to the solid bottom. LaRocque, Imran & Chaudhry (2013a) used an ultrasonic Doppler velocity profiler to measure the vertical distribution of the mean velocity at four different locations upstream of the removed gate. However, the vertical velocity profiles could not be measured on the downstream side due to the shallow depth of the wave flow. More recently, Wüthrich *et al.* (2018) performed laboratory measurements of a dam-break flow using an ultrasound profiler. They were able to measure velocity profiles behind the wavefront, which were found to be in good agreement with Prandtl's power law for open channel flows.

Numerically, clear-water dam-break flows have been mostly simulated using depth-averaged, 2-D models which solve the 2-D shallow water equations (SWEs) in discrete form (e.g. Fernández-Nieto, *et al.* 2010; Castro-Orgaz & Hager 2019; Bates 2022 Muchiri *et al.* 2024). Moreover, approximate analytical solutions have been proposed (e.g. Hogg & Pritchard 2004; Chanson 2009; Deng, Liu & Lu 2018). More recently, fully non-hydrostatic Navier–Stokes solvers were used to simulate dam-break flows. This approach leads to a more accurate description of the flow features compared with SWE-based models, especially when the vertical flow accelerations cannot be neglected, i.e. the pressure distribution is strongly nonhydrostatic. Both large eddy simulation (LES) and Reynolds-averaged Navier–Stokes (RANS) equations models have been used to predict

the temporal evolution of Newtonian dam-break flows (e.g. LaRoque *et al.* 2013*b*; Horna-Munoz & Constantinescu 2018, 2020; Maranzoni & Tomirotti 2023; Simsek & Islek 2023). Most of the Navier–Stokes simulations of dam-break flows were performed using an Eulerian framework in conjunction with the volume of fluid (VOF) method to capture the evolution of the water–air interface. The simulations were generally found to reproduce fairly well the experimental results in terms of the macro-scale properties of the dam-break flow for both dry- and wet-bed conditions (e.g. Horna-Munoz & Constantinescu 2020; Simsek & Islek 2023). Unfortunately, a detailed characterisation of the mean and turbulence quantities close to the solid wall has not been provided even in these studies.

Although mud is a mixture of solid and liquid phases, it has been frequently schematised as single-phase medium with non-Newtonian behaviour. In this framework, several rheological models have been used, based on the power law (e.g. Ng & Mei 1994) and on the Herschel–Burkley (e.g. Huang & Garcia, 1984) and Bingham (e.g. Liu & Mei 1989) rheological laws.

The present study is focused on a specific kind of mud, i.e. a clay–water mixture, whose rheology is commonly described through a shear-thinning power-law model. This type of mixture is frequently encountered in several natural settings. For example, Carotenuto *et al.* (2015) reported that the landslide in Cervinara (Italy) was a mixture of water and particles with diameters of the order of 10 μm . Zhang, Bai & Ng (2010), while discussing the natural estuarine muds dredged from Haihe River in Tianjin, concluded that 80 % of the particles had diameters smaller than 10 μm . Moreover, similar mixtures, i.e. slurries, are commonly found in mine wastes (Borger, 2013). When small-sized fine particles (typically with diameters less than 100 μm) are present, the mixture can exhibit pronounced non-Newtonian characteristics even at relatively low concentrations (Pierson 2005).

Dam-break waves of mud mixtures have been the object of several laboratory investigations, as reviewed recently by Aureli *et al.* (2023). For several mixtures with different rheology, the free surface, the wave front propagation and the wave front profiles have been recorded using video cameras. Due to the dimensions of the laboratory device in which the dam break was investigated and to the rheological characteristics of the employed mixtures, the dam-break flow was laminar in most of these experimental studies. Several analytical (e.g. Hogg & Pritchard 2004) and SWE numerical (e.g. Balmforth *et al.* 2007) studies investigated the characteristics of a mud dam-break wave. All these researchers assumed laminar flow conditions inside the wave and the validity of the long-wave approximation. The comparison with experimental results has shown that an SWE model, independently of the wave fluid rheology, is able to reproduce fairly well the macro-scale properties of the laminar dam-break wave of mud flow. More accurate numerical results were obtained by removing the hydrostatic pressure distribution assumption (e.g. see Shao & Lo 2003; Minussi & de Freitas Maciel, 2012; Liu *et al.* 2016; Schaer *et al.* 2018; Valette *et al.* 2021).

At field conditions, most mud flows are turbulent or weakly turbulent (Blight 1997; Pirulli *et al.* 2017). For this reason, understanding the hydrodynamic behaviour of mud dam-break flows generated in applications of engineering interest requires quantifying turbulence effects.

The motion of non-Newtonian fluids in turbulent uniform flow conditions has been the object of several investigations conducted in open channels, closed channels and pressurised conduits. For steady, turbulent flow conditions, experiments (Dodge and Metzner, 1959) have demonstrated that a unique correlation exists between the friction factor and the generalised Reynolds number for both polymeric solutions and solid (clay)–liquid suspensions. A similar conclusion was reached by Benslimane *et al.* (2016) who conducted experiments with a mixture of bentonite and water with concentrations

as high as 5 % ($n = 0.68$). Subsequently, Burger (2014) and Burger, Haldenwang & Alderman (2015) performed an extensive experimental investigation that considered open channels with different shapes and different clay water concentration to change the non-Newtonian rheology of the slurry. Using the acquired data sets, a generalised friction coefficient–Reynolds number correlation was proposed. Mitishita *et al.* (2021) carried out an experimental study of fully turbulent flow of a yield stress fluid in a rectangular duct. The experiments were performed at different Reynolds numbers and the turbulence statistics and power spectral densities of the velocity fluctuations were analysed. LES (e.g. Gnambo *et al.* 2015) and direct numerical simulations (DNS) at low Reynolds numbers (e.g. Karahan, Ranjan & Aidun 2023) have been used to obtain a detailed description of the wall-normal distributions of the mean velocity and of several turbulent quantities for fully developed (steady-mean) flow of non-Newtonian fluids. Fully developed, steady turbulent flows of slurries modelled as homogeneous single-phase fluids with non-Newtonian rheology have been investigated using RANS (Bartosik 2010), LES (Basso, Franco & Pitz 2022) and DNS (Singh *et al.* 2016).

To the best knowledge of the authors, the only numerical investigation that analysed the propagation of a turbulent dam-break wave of a power-law fluid is the recent study of Del Gaudio *et al.* (2024). The study focused on the physics of the impact of a dam-break wave containing a mixture of fine clay and water with a relatively low volume concentration of clay (i.e. $C_v < 10\%$) against a vertical rigid wall. The 3-D LES simulations were conducted using the dynamic Smagorinsky model. The VOF technique (Hirt & Nichols 1981) was used to capture the interface between the wave fluid and the surrounding air. The geometrical set-up was identical to that used in a series of experiments conducted with water, which were also used to validate the numerical model for Newtonian dam-break flows. Given the relatively short distance between the gate and the downstream wall, the simulations allowed studying only the first stages of the wave propagation in which turbulence effects were relatively small. Strong turbulence was generated once the wave started interacting with the vertical wall, which showed the advantages of using 3-D LES to investigate the physics of these flows. However, the physics and evolution of a turbulent dam-break wave of non-Newtonian fluid past its initial stages have not been investigated yet based on eddy-resolving simulations. Two other important research questions are: (i) to what extent can one-dimensional (1-D) shallow water models reproduce the main behaviour (e.g. front velocity, shape of the interface) of such dam-break waves of power law fluid in turbulent conditions?; and (ii) what features should the 1-D SWE model include to be able to accurately predict such flow characteristics from an engineering point of view?

Using the numerical approach proposed by Del Gaudio *et al.* (2024), the present paper aims to provide an in-depth analysis of turbulent dam-break waves of power-law fluids propagating in a long, wide and horizontal channel. Given that in practical applications such dam-break waves (e.g. mudflow waves) develop in very wide domains, the present simulations are conducted with no lateral walls. Rather the flow is assumed to be homogeneous in the spanwise direction, which also allows for calculating turbulence statistics (e.g. turbulent velocity fluctuations) at a given time instant. This set-up can be considered as a canonical configuration for this type of flow. This is the first time that 3-D LES is used to characterise the evolution and structure of turbulent Newtonian dam-break waves in this canonical set-up.

The paper discusses the effects of the rheological parameters (i.e. consistency index and power-law index) of the non-Newtonian power-law fluid on the macro-scale properties of the wave propagation (e.g. front velocity and the power-law regimes describing the temporal evolution of the front, the bed shear stress distributions) on the wave structure,

Case	$k \text{ (Pa s)}^n$	$n (-)$	$\rho \text{ (kg m}^{-3}\text{)}$	$\mu_0 \text{ (Pa s)}$	$h_0 \text{ (m)}$	$Re (-)$	$Re'_c (-)$
0	0.0009	1	1000	0.0009	0.2	3 10 000	2100
1	0.09	0.90	1064	0.0730	0.2	4023	2147
2	0.09	0.60	1064	0.0410	0.2	7210	2360
3	0.09	0.30	1064	0.0230	0.2	12 900	2790
4	0.09	0.10	1064	0.0160	0.2	19 104	3500
5	0.009	0.60	1064	0.0041	0.2	72 100	2360
6	0.0009	0.60	1064	0.0004	0.2	721 000	2360

Table 1. Main parameters of the test cases.

and on the vertical profiles of the mean streamwise velocity and Reynolds stresses inside the wave. The limiting case of a water dam-break flow is also considered to better highlight the differences between dam-break waves of Newtonian and non-Newtonian fluids. The LES data sets are also used to investigate the predictive abilities of 1-D SWE models which are extensively used for practical applications involving mudflows. In particular, a new 1-D SWE model is proposed based on the laminar model of Hogg & Pritchard (2004) in which the shape factor and the bottom stress assume turbulent conditions inside the power-law fluid. More specifically, the shape factor is assumed to be equal to one and the bottom stress is estimated using the empirical correlation of Dodge & Metzner (1959). Moreover, in the SWE framework, an approximate analytical solution of the dam-break problem is found by splitting the wave into an outer region, in which friction can be neglected, and an inner turbulent region, close to the front of the wave, where bed friction effects are important (Whitham 1955).

The 3-D LES model and the 1-D SWE models are described in § 2. The same section includes results of a grid dependency study conducted for LES and describes the geometrical and flow parameters of the Newtonian and non-Newtonian test cases. Section 3 discusses the flow and the turbulence structure inside the dam-break wave for both Newtonian and non-Newtonian fluids. Section 4 focuses on the temporal evolution of the front position and the associated wave propagation regimes based on numerical experiments conducted using 3-D LES. The same section uses the LES results to evaluate the predictive capabilities of SWE models in terms of their ability to correctly predict the front evolution, interface position and shape, and the bed shear stress and friction coefficient distributions. Finally, § 5 presents some final discussion and conclusions.

2. Test cases and numerical models

2.1. Test cases

The six test cases (table 1) discussed in the present study reproduce dam-break waves of non-Newtonian fluids with a high volume of release. The non-Newtonian fluids considered in the simulations are characterised by a power-law rheology with a consistency index, k , and power exponent, n . An additional test, Case 0, was conducted with a Newtonian fluid (water). In the following, k for Case 0 is equal to the water dynamic molecular viscosity.

The computation domain in the simulations is $L = 110h_0$ long, $B = 1.5h_0$ wide and $H = 1.5h_0$ high, where h_0 is the initial height of the lock region containing the wave fluid. The lock gate is situated at $x/h_0 = 0$ (figure 1). The length of the region containing the lock fluid at the start of the simulations is $60h_0$, with the floodable area extending to the right of the lock gate over a length of $50h_0$. This configuration allowed for the discharge to be maintained close to constant at the lock gate during the simulations.

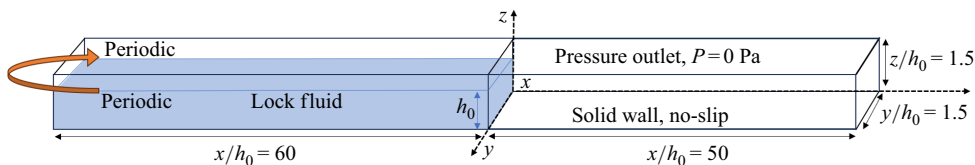


Figure 1. Sketch of the computational domain and its dimensions. View of the channel showing the initial location and depth, h_0 , of the wave fluid and the boundary conditions.

The spanwise width of the channel was sufficiently large for the width-averaged solution to be independent of the domain width and to capture the formation of a fairly large number of near-wall streaks.

As summarised in table 1, in the clear water case (Case 0), the density and dynamic molecular viscosity were $\rho = 1000 \text{ kg m}^{-3}$ and $k = 0.0009 \text{ Pa s}$, respectively. The non-Newtonian power-law fluids in the other six cases had a density $\rho = 1064 \text{ kg m}^{-3}$. Cases 1–4 considered power-law fluids characterised by four different rheological index values ($n = 0.1, 0.3, 0.6, 0.9$) and the same consistency index that was 100 times higher with respect to the water dynamic molecular viscosity (Case 0). Comparison of Cases 1, 2, 3 and 4 allows for studying the effect of varying the power-law index on the structure and propagation of the dam-break wave. Cases 5 and 6 have the same n value as for Case 2, but the k value is 10 and 100 times lower for Case 5 and Case 6, respectively, compared with Case 2. Comparison of Cases 2, 5 and 6 enables understanding the effect of varying the consistency index.

Results are presented in dimensionless form, considering the following length, time and velocity reference scales: h_0 , $t_0 = \sqrt{h_0/g}$ and $U_0 = \sqrt{gh_0}$, respectively, where g is the gravitational acceleration.

The reference Reynolds number is defined as

$$Re = \frac{\rho U_0 h_0}{\mu_0} = \frac{\rho U_0^{2-n} h_0^n}{k}, \quad (2.1)$$

where $\mu_0 = k(U_0/h_0)^{n-1}$ denotes the reference dynamic molecular viscosity for power-law fluids. In the clear water case, μ_0 denotes the (water) dynamic viscosity. For uniform conditions in a wide channel, i.e. two-dimensional steady parallel flow conditions, a Reynolds number $Re' = (\rho V_u D)/(\mu_0)$ can be defined with the hydraulics diameter $D = 4h_u$, where h_u is the uniform flow depth and V_u is the corresponding depth-averaged streamwise velocity. The critical Reynolds number value for which the flow remains laminar is (Mishra & Tripathi 1971)

$$Re'_c = 2100 \frac{(4n+2)(5n+3)}{3(3n+1)^2}. \quad (2.2)$$

Although (2.2) is strictly valid for uniform flow conditions, the Re'_c value is assumed to be fairly representative of critical conditions even for unsteady (e.g. dam break) flows. The values of Re and Re'_c for each case are also included in table 1.

2.2. LES solver, grid dependency study and model validation

The numerical model is the one described by Del Gaudio *et al.* (2024) who performed similar LES of dam-break waves in more complex geometries. The governing equations are the (filtered) Navier–Stokes equations and the advection equation for the volume fraction of wave fluid, which is used to track the interface between the wave fluid and

the surrounding air in the VOF–LES simulations. To maintain a sharp interface, a high-resolution interface capturing scheme is employed (HRIC). The filtered continuity and momentum equations are

$$\frac{\partial u_j}{\partial x_j} = 0, \quad (2.3)$$

$$\rho \frac{\partial u_i}{\partial t} + \rho \frac{\partial u_i u_j}{\partial x_j} = -\frac{\partial p}{\partial x_i} + \frac{\partial}{\partial x_j} \left[\mu \left(\frac{\partial u_i}{\partial x_j} + \frac{\partial u_j}{\partial x_i} \right) \right] - g \delta_{i,3} - \frac{\partial \sigma_{ij}}{\partial x_j}, \quad (2.4)$$

where p and u_i represent the dimensional filtered pressure and Cartesian velocity component in the i direction, respectively. In (2.4), $\delta_{i,k}$ denotes the Kronecker delta function, and x_1, x_2, x_3 correspond to the x, y and z variables, respectively. Assuming a power law as the constitutive relation, the dynamic molecular viscosity is

$$\mu = k (S_{ij} S_{ij})^{\frac{n-1}{2}}, \quad (2.5)$$

where S_{ij} is the filtered velocity deformation (rate of strain) tensor:

$$S_{ij} = \frac{1}{2} \left(\frac{\partial u_i}{\partial x_j} + \frac{\partial u_j}{\partial x_i} \right). \quad (2.6)$$

The molecular viscosity tends to infinity near the free surface for a power-law fluid. Following Gnamonde *et al.* (2015), we limited the Frobenius norm of the velocity deformation tensor to bound the molecular viscosity. A cut off value of 10^{-4} was used. The subgrid stress tensor, σ_{ij} , is calculated using the dynamic Smagorinsky model (Rodi, Constantinescu & Stoesser 2013; Gnamonde *et al.* 2015). Its expression is $\sigma_{ij} = -2\nu_t S_{ij} = -2C_d \Delta^2 |S| S_{ij}$, where ν_t is the turbulent subgrid scale (eddy) viscosity, Δ is the local grid spacing, $|S|$ is the magnitude of S_{ij} and C_d is the model parameter that is dynamically calculated using information available from the smallest resolved scales (Rodi *et al.* 2013).

The VOF free surface tracking technique was successfully applied to simulate dam-break and flood-wave flows (e.g. see Horna-Munoz & Constantinescu 2018, 2020). A pure-advection equation is solved for the volume fraction of water (η): $(\partial \eta / \partial t) + u_j (\partial \eta / \partial x_j) = 0$. In cells containing only water, $\eta = 1$. In cells containing only air, $\eta = 0$. A value of 0.5 was chosen for η to visualise the interface and determine the front position in LES.

The SIMPLE (semi-implicit method for pressure linked equations) algorithm is used to integrate the discretised Navier–Stokes equations that are advanced in time using a semi-implicit, iterative method. The third-order MUSCL scheme is used to discretise the advective terms, the second-order central-differences scheme is used to discretise the diffusive and pressure gradients terms, and a second-order accurate scheme is used to discretise the time derivatives in the governing equations. A pressure outlet boundary condition with a zero volume fraction of the liquid phase and a pressure of 0 Pa is specified at the top boundary. No-slip conditions (i.e. zero velocity) are imposed at the bottom boundary (horizontal channel bed) and at the left boundary. The flow is assumed to be periodic in the spanwise (y) direction. The initial velocity field is set to zero and the lock gate is removed instantaneously at $t = 0$. The time step is the same for all simulations and it corresponds to a Courant number close to 0.2 away from the channel bed.

A finer mesh was used in regions situated close to the channel bottom, such that the attached boundary layers and the velocity gradients were well resolved. The Cartesian-like, unstructured mesh was refined near this boundary using 15 prism layers. This allowed for placing the first point off the surface of the channel bottom at approximately three wall units for the highest Reynolds number simulation. No wall functions were used.

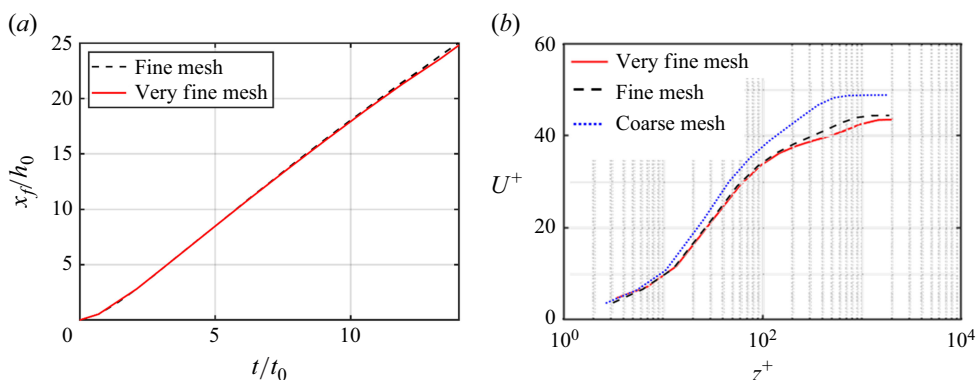


Figure 2. Grid dependency study for Case 5. (a) Non-dimensional temporal variation of the front position; (b) non-dimensional streamwise velocity profile at section $x/h_0 = 12.5$ when the front is situated at $x_f/h_0 = 25$. The very fine mesh contains 25 million cells, the fine mesh contains 18 million cells and the coarse mesh contains 9 million cells.

The spanwise and streamwise sizes of a typical computational cell were of the order of 20–30 wall units. Two hundred grid points were used to discretise the domain along the spanwise direction. The total number of grid cells was close to 18 million for all the simulations.

A grid sensitivity analysis was conducted. As an example, results for Case 5 are discussed. Figure 2 shows the temporal evolution of the dimensionless front position, x_f/h_0 , and the profile of the spanwise averaged velocity at $x/h_0 = 12.5$ and $x_f/h_0 = 25$ in wall coordinates ($U^+ = U/u_\tau$ and $z^+ = zu_\tau/\nu_w$, where $U(x, z)$ is the dimensional spanwise averaged velocity profile, $u_\tau(x)$ is the local bed friction velocity and $\nu_w(x)$ is the kinematic molecular viscosity at the channel bed). The temporal evolution of the front position (figure 2a) is close to identical in the simulations conducted with grids containing 18 million cells and 25 million cells. Significant differences are observed between the velocity profiles in figure 2(b) corresponding to the simulation performed using a coarse mesh containing close to 9 million cells and the two other simulations conducted on meshes containing more than 18 million cells. The velocity profiles inside the dam-break wave and the front velocity in the two finer-mesh simulations are very close. So, one can conclude that simulations performed using meshes with at least 18 million cells are grid independent. The slope of the logarithmic region in the two finer-mesh simulations is larger than the one expected for a Newtonian fluid (e.g. water). This behaviour is consistent with previous findings by Gnambonde *et al.* (2015) for non-Newtonian shear-thinning fluids.

The solver (STARCCM+) was extensively validated for turbulent flows involving Newtonian fluids (water). In particular, the solver was shown to accurately predict unsteady free surface flows in RANS-VOF simulations with a deformable free surface (e.g. Horna-Munoz & Constantinescu 2018, 2020). Del Gaudio *et al.* (2024) compared free surface deformation and wall pressures from 3-D LES of a water dam-break wave impacting a vertical wall with laboratory experimental data. Very good agreement between experimental data and LES predictions was observed for these variables. In the same study, the non-Newtonian fluid rheology solver was validated using data from the dam-break experiments conducted by Minussi & Maciel (2012). In terms of non-dimensional wall units, the level of mesh refinement in the present simulations is similar to that used by Del Gaudio *et al.* (2024) in their dam-break simulations conducted with Newtonian and non-Newtonian fluids.

2.3. Shallow water models

2.3.1. Governing equations

Considering a homogeneous layer of fluid flowing over a horizontal bed, without lateral inflow or outflow, assuming that spatial variations occur over scales larger than the flow depth, and that flow resistance due to the sidewalls and surface tension effects are negligible, the dimensional depth-averaged momentum and mass conservation equations are (Hogg & Pritchard 2004)

$$\frac{\partial V}{\partial t} + \beta \frac{\partial h V^2}{\partial x} + gh \frac{\partial h}{\partial x} + \frac{\tau_b}{\rho} = 0, \quad (2.9)$$

$$\frac{\partial h}{\partial t} + \frac{\partial(Vh)}{\partial x} = 0, \quad (2.10)$$

where h is the flow depth, V is the depth-averaged velocity, β is the shape factor and τ_b is the bottom shear stress. Independently of the fluid rheology and flow conditions, i.e. laminar or turbulent, β and τ_b are evaluated assuming that the shape of vertical velocity profile corresponds to uniform conditions. For a power-law fluid and laminar flow conditions, the expressions for the shape factor and the bottom shear stress are (Ng & Mei 1994)

$$\beta = 2 \frac{2n+1}{3n+2} \quad \tau_b = k \left(\frac{2n+1}{n} \frac{V}{h} \right)^n. \quad (2.11)$$

For clear water and turbulent flow conditions, a unitary value of the shape factor is assumed, and the bottom shear stress is expressed as

$$\tau_b = \rho C_f V^2, \quad (2.12)$$

where C_f is the friction coefficient. For turbulent flow of a Newtonian fluid over a rough boundary and at high Reynolds number, a constant value is generally assumed for the friction coefficient (Hogg & Pritchard 2004). By contrast, for turbulent flow over a smooth bottom, C_f may be evaluated using the empirical Blasius formula (Blasius, 1913). In the case of a wide-open domain, i.e. assuming the hydraulic diameter is equal to four times the flow depth, it reads

$$C_f = \frac{0.316}{8} \left[\frac{\mu_0}{4\rho Vh} \right]^{1/4}. \quad (2.13)$$

Similarly to the clear water case, to deal with power-law fluids in turbulent flow conditions, we assume a unitary value of the shape factor. Moreover, the bottom shear stress is evaluated using (2.12) with the friction coefficient given by the correlation of Dodge & Metzner (1959) modified for wide open channels:

$$C_f = \frac{a_n}{2} \left[\frac{k}{\rho} \frac{\left(6 + \frac{2}{n}\right)^n}{2^{2n+3} V^{2-n} h^n} \right]^{b_n} \quad (2.14)$$

with

$$a_n = 0.0665 + 0.01175n, \quad b_n = 0.365 - 0.177n + 0.062n^2. \quad (2.15)$$

2.3.2. Numerical solutions of the SWE

The SWE solution of the dam-break problem has been found by solving the nonlinear hyperbolic system of (2.9)–(2.10), assuming either laminar or turbulent flow conditions

LES	Large eddy simulation
SM-LN	Shallow model, laminar numerical
SM-TN	Shallow model, turbulent numerical
SM-TA	Shallow model, turbulent analytical
HM-LA	Hogg <i>et al.</i> 2004 model, laminar analytical

Table 2. Acronyms of the different numerical and theoretical models.

inside the dam-break wave. A second-order (in space and in time) finite-volume scheme was employed. The numerical fluxes were evaluated using the Harten–Lax–Van Leer (HLL) scheme (Harten, Lax & van Leer 1983). To guarantee the second-order spatial accuracy of the scheme, the values of the conserved variables at the two sides of the interface were estimated using a piecewise linear reconstruction scheme with a nonlinear min-mod limiter (LeVeque, 2011). Time integration was performed using the second-order, two-step Runge–Kutta scheme (Gottlieb & Shu 1998). At the outlet, a nonlinear non-reflecting characteristic boundary condition was prescribed (Nycander, Hogg & Frankcombe 2008). Additional details about the numerical scheme can be found from Campomaggiore *et al.* (2016). In what follows, the numerical results of the SWE model corresponding to laminar and turbulent flow conditions inside the wave are denoted SM-LN and SM-TN, respectively (table 2).

2.3.3. Novel analytical solution for a turbulent dam-break wave of a power-law fluid

The theoretical modelling of dam-break flows in canonical configurations (e.g. wide horizontal channel, 2-D flow) based on analytically integrating the SWE equations (2.9)–(2.10) with some additional assumptions has been the object of several studies. The first approximate analytical solution, derived by Ritter (1982), neglects the bottom resistance and assumes $\beta = 1$. Approximate analytical solutions for turbulent clear-water dam-break waves have been proposed (e.g. Hogg & Pritchard 2004; Chanson 2009). Moreover, an analytical solution for a laminar dam break wave of a power-law fluid was derived by Hogg & Pritchard (2004). In the next sections, the analytical solution by Hogg & Pritchard (2004) for a dam-break wave of a laminar power-law fluid will be identified with the label HM-LA.

In the present section, an approximate analytical solution for an instantaneous-release dam-break wave of turbulent power-law fluid propagating in a horizontal, wide channel is deduced. The new solution is based on the conceptual model of Whitham (1955) and can be thought as the generalisation for turbulent power-law fluids of Chanson's (2009) solution valid for a turbulent dam-break wave of clear water. To this aim, considering the reference length, time and velocity scales previously indicated (i.e. h_0 , $t_0 = \sqrt{h_0/g}$ and $U_0 = \sqrt{gh_0}$), the following dimensionless quantities are defined:

$$\tilde{x} = \frac{x}{h_0}; \quad \tilde{t} = \frac{t}{t_0}; \quad \tilde{h} = \frac{h}{h_0}; \quad \tilde{V} = \frac{V}{U_0}. \quad (2.16)$$

The SWE model for a turbulent power-law fluid, consisting of (2.9) (assuming $\beta = 1$), (2.10), (2.12), (2.14) and (2.15) is rewritten in dimensionless form as follows:

$$\frac{\partial \tilde{V}}{\partial \tilde{t}} + \tilde{V} \frac{\partial \tilde{V}}{\partial \tilde{x}} + \frac{\partial \tilde{h}}{\partial \tilde{x}} + \tilde{C}_f \frac{\tilde{V}^\lambda}{\tilde{h}^\phi} = 0, \quad (2.17)$$

$$\frac{\partial \tilde{h}}{\partial \tilde{t}} + \tilde{V} \frac{\partial \tilde{h}}{\partial \tilde{x}} + \tilde{h} \frac{\partial \tilde{V}}{\partial \tilde{x}} = 0, \quad (2.18)$$

in which

$$\tilde{C}_f = \frac{a_n}{2} \left[\frac{k}{\rho} \frac{\left(6 + \frac{2}{n}\right)^n}{2^{2n+3} U_0^{2-n} h_0^n} \right]^{b_n}; \quad \lambda = b_n (n-2) + 2; \quad \phi = n b_n + 1, \quad (2.19)$$

and the expressions of the coefficients a_n and b_n are given by (2.15).

Following Whitham (1955), the turbulent dam-break wave of a power-law fluid is analysed by splitting the solution domain into an outer region, $-\infty < \tilde{x} \leq \tilde{x}_1$, in which the friction is neglected (inviscid fluid), and an inner region, close to the wave front, $\tilde{x}_1 < \tilde{x} \leq \tilde{x}_s$, where the effects of bottom friction are important. The streamwise lengths \tilde{x}_1 and \tilde{x}_s denote the dimensionless position of the inviscid–turbulent interface and the wave front position, respectively. Both quantities are unknown and vary with time.

In the outer region, where bottom friction is neglected (inviscid fluid), the solution of (2.17) and (2.18) is the well-known Ritter’s solution (Ritter 1892):

$$\tilde{h}_I = \frac{1}{9} \left(2 - \frac{\tilde{x}}{\tilde{t}} \right)^2 \quad -\infty < \tilde{x} \leq \tilde{x}_1, \quad (2.20a)$$

$$\tilde{V}_I = \frac{2}{3} \left(1 + \frac{\tilde{x}}{\tilde{t}} \right), \quad (2.20b)$$

with the wave front travelling with a dimensionless celerity $\tilde{U}_{f,I}$ equal to two. The subscript ‘I’ denotes the inviscid region. Considering that the velocity does not spatially vary inside the inner region, its value can be assumed to be equal to the (unknown) wave front velocity \tilde{U}_f (Chanson 2009). Therefore, assuming that the acceleration and the inertial terms are negligible with respect to the flow resistance inside the inner region, (2.17) reduces to the diffusive equation:

$$\frac{\partial \tilde{h}_D}{\partial \tilde{x}} + \tilde{C}_f \frac{\tilde{U}_f^\lambda}{\tilde{h}_D^\phi} = 0, \quad \tilde{x}_1 \leq \tilde{x} \leq \tilde{x}_s. \quad (2.21)$$

Integrating (2.21) between \tilde{x}_1 and \tilde{x}_s , and imposing the boundary condition $\tilde{h}_D(\tilde{x}_s) = 0$, leads to the following inner region approximate solution:

$$\tilde{h}_D = \left[\tilde{C}_f (\phi + 1) \tilde{U}_f^\lambda \right]^{\frac{1}{1+\phi}} (\tilde{x}_s - \tilde{x})^{\frac{1}{1+\phi}} \quad \tilde{x}_1 \leq \tilde{x} \leq \tilde{x}_s \quad (2.22a)$$

assuming

$$\tilde{V}_D = \tilde{U}_f. \quad (2.22b)$$

The subscript ‘D’ is used for variables inside the turbulent region that are calculated by solving the diffusive (2.21). Imposing that the inner and outer domain solutions coincide at the interface between the two regions ($\tilde{h}_I(\tilde{x}_1) = \tilde{h}_D(\tilde{x}_1)$ and $\tilde{V}_I(\tilde{x}_1) = \tilde{V}_D(\tilde{x}_1) = \tilde{U}_f$) leads to the following expressions for \tilde{x}_1 and \tilde{x}_s :

$$\tilde{x}_1 = \frac{1}{2} (3\tilde{U}_f - 2) \tilde{t}, \quad (2.23a)$$

$$\tilde{x}_s = \frac{1}{2\tilde{C}_f (\phi + 1)} \left[\tilde{U}_f^{-\lambda} 2^{-2\phi-1} (2 - \tilde{U}_f)^{2\phi+2} + \tilde{C}_f (\phi + 1) (3\tilde{U}_f - 2) \tilde{t} \right]. \quad (2.23b)$$

Equations (2.23a) and (2.23b) allow for calculating $\tilde{x}_1(t)$ and $\tilde{x}_s(t)$, provided that the wave front velocity \tilde{U}_f is known. The latter is evaluated by imposing mass conservation,

i.e. the mass of wave fluid in the inner region ($\tilde{x}_1 < \tilde{x} \leq \tilde{x}_s$) must be equal to the mass of ideal (inviscid) fluid in the corresponding front region $\tilde{x}_1 \leq \tilde{x} \leq \tilde{U}_{f,I}\tilde{t}$:

$$\int_{\tilde{x}_1}^{\tilde{x}_s} \tilde{h}_D dx = \int_{\tilde{x}_1}^{\tilde{U}_{f,I}\tilde{t}} \tilde{h}_I dx, \quad (2.24)$$

with $\tilde{U}_{f,I} = 2$.

Using (2.20a), (2.22a), (2.23a) and (2.23b), the following relationship between the dimensionless time and the wave front velocity \tilde{U}_f is obtained:

$$\tilde{C}_f (2 + \phi) \tilde{t} = \tilde{U}_f^{-\lambda} \left(1 - \frac{\tilde{U}_f}{2} \right)^{2\phi+1}. \quad (2.25)$$

For each time \tilde{t} , the iterative solution of (2.25) provides the value of \tilde{U}_f . Then, \tilde{x}_s and \tilde{x}_1 are calculated using (2.23b) and (2.23a), respectively. Once \tilde{U}_f , \tilde{x}_s and \tilde{x}_1 are known, the free-surface profiles can be calculated using (2.20a) for $-\infty < \tilde{x} \leq \tilde{x}_1$ and (2.22a) for $\tilde{x}_1 \leq \tilde{x} \leq \tilde{x}_s$.

The present analytical solution for turbulent clear water can be applied for analysing the wave propagating over a smooth wall by accounting for the friction coefficient variability along the current (Chanson 2009). Indeed, by adopting the Blasius formula (2.13) to estimate the friction coefficient, the analytical solution of a dam-break wave propagating over a smooth bed is given by (2.25), (2.20a) and (2.22a) assuming

$$\tilde{C}_f = \frac{0.316}{8} \left[\frac{\mu_0}{4\rho U_0 h_0} \right]^{1/4} \quad \lambda = 7/4 \quad \phi = 5/4. \quad (2.26)$$

In the next sections, the SW analytical solution of a turbulent dam-break wave of clear water and power-law fluid propagating over a smooth bed will be identified with the label SM-TA.

As a final remark, we point out that because $0 \leq \tilde{U}_f \leq 2$, one can deduce two asymptotic expressions of the front velocity valid for high and respectively for low values of the wave front velocity. It is worth pointing out that high/low values of the wave front celerity correspond to small/high values of the time. Indeed, for high \tilde{U}_f values (i.e. close to 2), the second term on the right-hand side of (2.25) tends to vanish, while the first term remains bounded. For such conditions, (2.25) may be approximated as follows:

$$\tilde{C}_f (2 + \phi) \tilde{t} = \left(1 - \frac{\tilde{U}_f}{2} \right)^{2\phi+1}. \quad (2.27)$$

The front velocity can then be calculated as

$$\tilde{U}_f = 2 - \left[\tilde{C}_f (2 + \phi) \tilde{t} \right]^{\frac{1}{2\phi+1}}. \quad (2.28)$$

Meanwhile, for small \tilde{U}_f values (i.e. close to 0), the second term on the right-hand side of (2.25) remains finite, while the first term tends to diverge. For such conditions, the approximation of (2.25) becomes

$$\tilde{C}_f (2 + \phi) \tilde{t} = \tilde{U}_f^{-\lambda}, \quad (2.29)$$

which leads to the following expression of the wave front velocity:

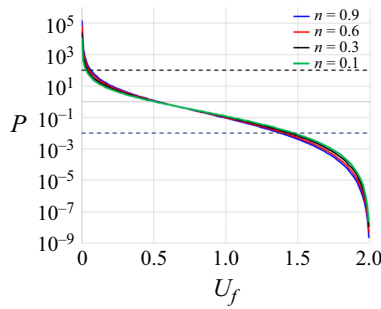


Figure 3. Variation of the P ratio (2.31) with the wave front velocity, \tilde{U}_f , for different values of the rheological index, n .

$$\tilde{U}_f = \left(\frac{1}{\tilde{C}_f (2 + \phi) \tilde{t}} \right)^{\frac{1}{\lambda}}. \quad (2.30)$$

To better illustrate this behaviour, one can consider the ratio between the two terms on the right-hand side of (2.25):

$$P = \frac{\left(1 - \frac{U_f}{2}\right)^{2\phi+1}}{U_f^\lambda}. \quad (2.31)$$

The value of this ratio indicates which of the two terms is predominant and, based on this, which of the two approximate solutions given by (2.27) and (2.29) should be applied. Figure 3 reports the P ratio as a function of the wave front velocity, \tilde{U}_f , for several values of the rheological index, n . Results indicate only a weak variability of P with n . Moreover, figure 3 can be used to estimate the applicability range of the two limiting expressions deduced for \tilde{U}_f , i.e. (2.28) and (2.30). Assuming that a difference of two orders of magnitude allows neglecting one term with respect to the other one on the right-hand side of (2.25), the lower and upper bounds for the applicability of (2.28) and (2.30) are $\tilde{U}_f^{\min} = 1.4 \div 1.5$ and $\tilde{U}_f^{\max} = 0.03 \div 0.06$, respectively. In terms of the propagation time, the maximum time when the asymptotic solution given by (2.28) is valid, \tilde{t}^{\max} , and the minimum time after which the asymptotic solution given by (2.30) is valid, \tilde{t}^{\min} , can be found using (2.25) and setting $\tilde{U}_f = \tilde{U}_f^{\min}$ and $\tilde{U}_f = \tilde{U}_f^{\max}$, respectively.

Compared with the SM-TN numerical solutions that are based on solving the full shallow water equations, the newly proposed analytical model shows significantly better agreement in terms of the predicted free-surface profiles compared with those given by the classical Ritter solution for non-Newtonian cases. The new analytical model slightly underpredicts the front speed given by the SM-TN solution. The effect is stronger for low values of n . The new analytical model correctly predicts the shape of the dam-break wave near its front for all n values. Moreover, for values of n between 0.3 and 0.9, the free surface profiles predicted by the new analytical model and by the corresponding SM-TN solution are in good quantitative agreement over the whole length of the wave.

3. Flow and turbulence structure inside the dam-break wave

The main goal of this section is to investigate flow and the turbulent structure of high volume of release turbulent dam-break waves with a Newtonian and a non-Newtonian

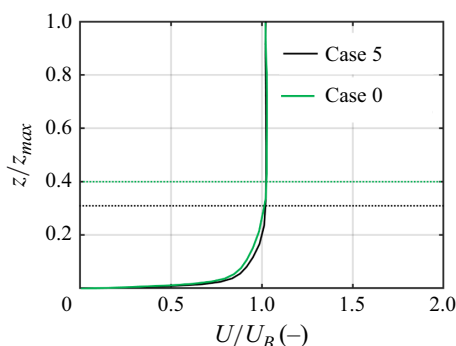


Figure 4. Streamwise (spanwise-averaged) velocity profiles for Case 0 ($n = 0$) and Case 5 ($n = 0.6$) at $x/h_0 = 12.5$ when the front is situated at $x_f/h_0 = 25$. The dotted lines mark the start of the constant velocity layer.

rheology. Given the unsteady nature of these flows, very little information is available from experimental investigations on the vertical profiles of the streamwise velocity and Reynolds stresses inside the wave. Of particular interest is to investigate whether, or not, the velocity profile inside the wave region where the flow is turbulent resembles that observed in Newtonian turbulent boundary layers over a horizontal bed or in fully developed open channel flow where a logarithmic region is present until close to the edge of the boundary layer or the free surface of the open channel. A first important finding of the present numerical experiments conducted with both Newtonian and non-Newtonian fluids is the existence of a close to constant streamwise velocity layer at the interface between the wave and the surrounding air ($z = z_{max}$) and some variable vertical location inside the wave. Figure 4 shows the vertical profiles of the (spanwise-averaged) streamwise velocity component at a streamwise location situated behind the front. The velocity is normalised using the depth and spanwise averaged velocity near the top of the wave, $UB(x, t)$. The profiles show such a layer is present for both Newtonian (Case 0) and non-Newtonian (Case 5) dam-break waves. As will be discussed in the next two subsections, for both Newtonian and non-Newtonian cases, a logarithmic velocity layer is present beneath the constant velocity layer in the region where the flow inside the wave is turbulent, but the slope of the log law for the velocity profiles at different locations along the wave is generally different from that observed in turbulent, steady boundary layers of Newtonian fluids and varies with the distance from the front.

3.1. Newtonian dam-break wave

Case 0 is used to illustrate the internal flow structure for a dam-break wave of Newtonian fluid (water) where the flow is strongly turbulent inside the wave. The streamwise velocity increases fairly monotonically inside the wave as the front is approached (figure 5a), which means the turbulence will be stronger in regions situated closer to the wave front. Three-dimensional turbulent flow structures are present along the entire wave at the air–fluid interface. These structures are driven by the mean shear between the wave fluid and the surrounding air. As for the well-documented case of gravity currents (e.g. see Constantinescu 2014; Tokyay, Constantinescu & Meiburg 2012; Dai & Huang 2022), the instabilities present near the front of the wave generate lobe and cleft structures (figures 5b and 5c). Such structures were already observed for high-Reynolds-number dam-break waves by Del Gaudio *et al.* (2024) for the case of waves propagating into a channel of limited width. The absence of sidewalls in the present simulations conducted with periodic

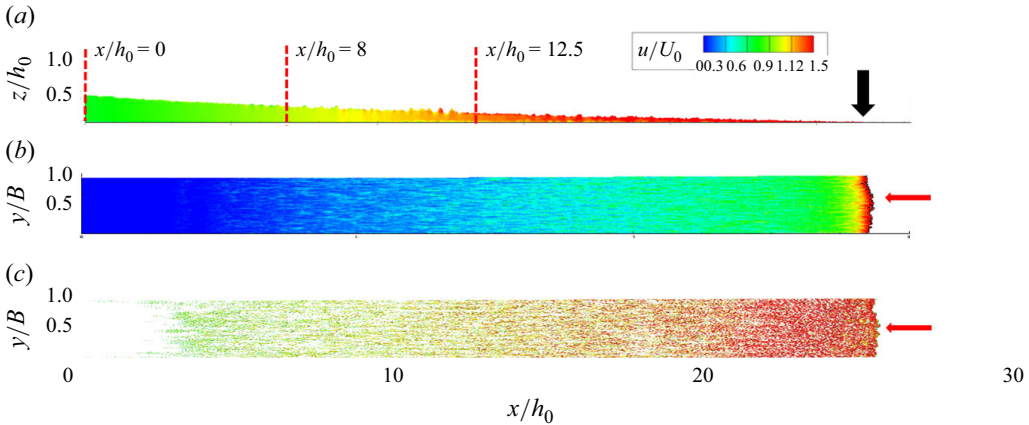


Figure 5. Visualisation of the instantaneous flow structure of the dam-break wave for Case 0. (a) Non-dimensional streamwise velocity in the vertical plane $y/B = 0.5$; (b) streamwise non-dimensional velocity component in a horizontal plane situated at approximately 20 wall units from the channel bed; (c) near-wall streaks visualised using a Q iso-surface ($Q = 500$). The black arrow shows the position of the front of the wave ($x_f/h_0 = 25$). The red arrows point towards the lobes and cleft structures at the front. The vertical red dashed lines show the locations of the velocity and turbulent shear stresses profiles in Figure 6.

boundary conditions in the spanwise direction does not have a significant effect on the development of these structures at the front of the wave.

Figures 5(b) and 5(c) also reveal the presence of near-bed coherent structures in the form of parallel streaks of higher and lower streamwise velocity near the channel bed, similar to those observed in turbulent boundary layers and fully developed turbulent flows in open channels. In the case of a turbulent dam-break flow, the streaks extend for some finite distance behind the front and gradually vanish at large distances from the front (e.g. see figures 5(b) and 5(c) where streaks are not present for $x/h_0 < 5$). This happens because, far from the wave front, the mean streamwise velocity inside the wave is not large enough to generate a sufficiently strong turbulent flow that can result in the formation of near-bed streaks. The average width of the streaks is close to 500 wall units ($\sim 0.05B$). So, these streaks are much larger in terms of their wall unit dimensions compared with those observed in fully turbulent boundary layers and channel flows. This is expected, as the flow conditions behind the front of the current are not exactly equivalent to those in the aforementioned statistically steady turbulent flows. Such large streaks were also observed behind the front of Newtonian high-Reynolds-number gravity currents in the large eddy simulations of Ooi, Constantinescu & Weber (2009) and Tokyay & Constantinescu (2015). Given the reduced height of the wave close to the front, the streaks of high and low velocity affect the flow structure until close to the wave interface inside this region.

The flow structure inside turbulent dam-break waves is investigated based on the spanwise-averaged streamwise velocity profiles and primary turbulent shear stress profiles, $\overline{u'w'}$, where the overbar denotes spanwise averaging and the velocity fluctuations in the streamwise and vertical directions are denoted u' and w' , respectively. A log-law region is present inside the turbulent dam-break wave in Case 0 (figure 6a–6c). The non-dimensional spanwise-averaged streamwise velocity profiles are plotted in inner coordinates at three streamwise locations extending from the lock gate to $x/h_0 = 12.5$ at the time when the front is situated at $x_f/h_0 = 25$. The vertical coordinate in wall units is $z^+ = z u_\tau(x)/\nu_w(x)$. In Case 0, $\nu_w(x)$ is a constant equal to the kinematic molecular viscosity of the water. Each velocity profile displays two main distinct regions: a boundary layer

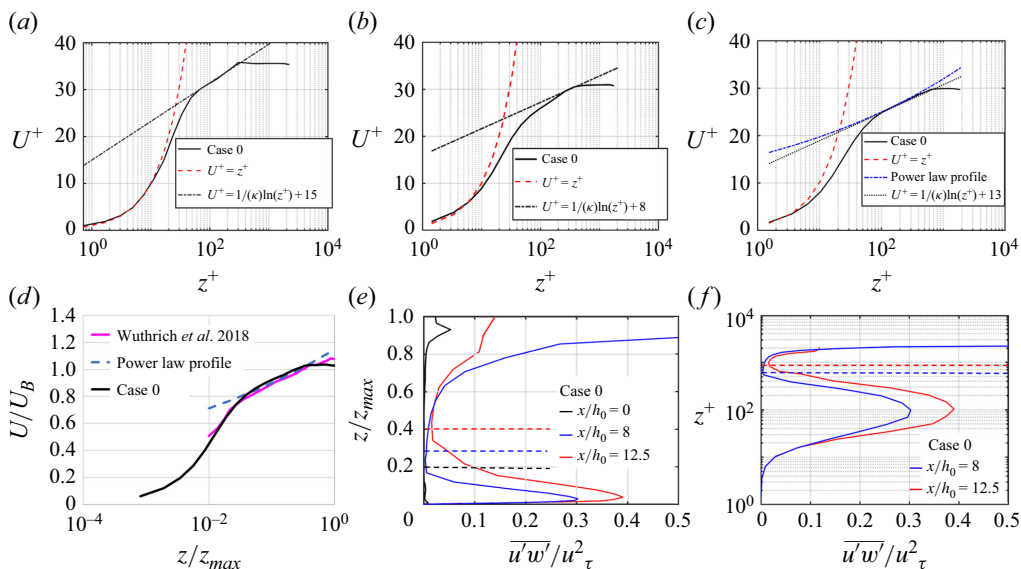


Figure 6. Vertical profiles of the non-dimensional mean streamwise velocity and primary turbulent shear stress, $\overline{u'w'}$, for Case 0. Results are shown when the front is situated at $x_f/h_0 = 28$. (a) Streamwise (spanwise-averaged) velocity profile at $x/h_0 = 0$ (lock gate), $\kappa = 0.28$; (b) streamwise (spanwise-averaged) velocity profile at $x/h_0 = 8$, $\kappa = 0.28$; (c) streamwise (spanwise-averaged) velocity profile at $x/h_0 = 12.5$, $\kappa = 0.40$; (d) comparison of Case 0 velocity profile at $x/h_0 = 12.5$ with velocity profile measured by Wuthrich *et al.* (2018). The blue dashed line corresponds to a power-law profile, $U/U_B = (h/H)^{1/8}$; (e) $\overline{u'w'}$ profiles; (f) $\overline{u'w'}$ profiles in wall coordinates. The horizontal dotted lines in panels (e) and (f) correspond to the boundary between the logarithmic layer and the constant velocity layer of the dam-break wave.

containing the wall viscous, buffer and log-law (sub) layers followed by a constant velocity layer that extends up to the wave interface with the air (see also discussion of figure 4). At the lock gate (figure 6a), where turbulence is weak, the thickness of the viscous sublayer is large as it extends up to approximately 20 wall units away the bed surface. The viscous sublayer extends up to approximately 5 wall units at the other two streamwise locations where the turbulence is much stronger (figure 6e) and velocity streaks are present. The main observation related to the presence of a log-law layer in Newtonian dam-break flows is that the slope of the logarithmic velocity profile (i.e. $1/\kappa$) decreases with the distance from the lock gate. The velocity profiles at $x/h_0 = 0$ and 8 suggest a value of κ close to 0.28. However, in the near-front region of high streamwise velocity and strong turbulence, κ approaches to the von Kármán constant value associated with steady turbulent flows (e.g. $\kappa \approx 0.4$ at $x/h_0 = 12.5$ in figure 6c). In this region of strong turbulence, the log-layer extends over close to 40 % of the wave height, z_{max} (see also Case 0 velocity profile in figure 4).

Figure 6(d) shows that the predicted non-dimensional velocity profile at $x/h_0 = 12.5$ in Case 0 is in good qualitative agreement with that measured in a lab experiment conducted by Wuthrich *et al.* (2018) for a turbulent dam-break wave propagating over a smooth, horizontal channel. Wuthrich *et al.* (2018) showed that their streamwise velocity profiles were well approximated by a power-law function with an exponent of $1/8$, which also corresponds to a log-law region with a value of κ close to 0.4. At larger distances from the bed, the velocity inside the wave was close to constant. The $1/8$ power-law profile also provides a good approximation of the numerically predicted velocity profiles inside the log-law layer in the region where the flow inside the wave is strongly turbulent (e.g. see figure 6c).

Near the lock gate, where turbulence is weak, turbulent shear stresses are found to be negligible (see profile of the primary turbulent shear stress $\overline{u'w'}$ at $x/h_0 = 0$ in [figure 6e](#)). In the near-front region, where the turbulence inside the wave is strong (e.g. at $x/h_0 = 12.5$ in [figure 6f](#)), the peak of $\overline{u'w'}$ occurs at approximately 100 wall units, which is comparable to the distance where the log-law layer starts of approximately 80 wall units ([figure 6c](#)). This behaviour is consistent with what is observed in turbulent boundary layers and fully developed open channel flows. At higher elevations, the turbulent shear stresses decay monotonically with increasing distance from the smooth bed and reach a minimum value slightly above the interface between the log-law layer and the constant velocity layer. Interestingly, despite the fact that the mean streamwise velocity is close to constant, the shear stress inside the constant velocity layer increases as the wave–air interface is approached. This is consistent with the presence of smaller-scale deformations along this interface in [figure 5\(a\)](#).

3.2. Non-Newtonian dam-break wave

Case 5, which is characterised by a relatively high Reynolds number ($Re = 7.2 \times 10^4$, $Re_{MR} = Re = 2.73 \times 10^5$), is used to discuss the spanwise-averaged flow and turbulence structure inside non-Newtonian dam-break waves. Case 5 shows many similarities with Case 0 representing a Newtonian dam-break wave. For example, the friction-velocity Reynolds numbers at $x/h_0 = 12.5$ are very close in the two simulations ($Re_\tau \approx 500$, where $Re_\tau = u_\tau \delta / \nu_w$ and δ is the local thickness of the boundary layer).

[Figures 7\(a\)](#) and [7\(b\)](#) show the presence of a log-law region inside the non-Newtonian dam-break wave. As for the case of a wave of Newtonian fluid, turbulence is very weak near the lock gate in Case 5, as illustrated by the very low values of the primary turbulent shear stress at $x/h_0 = 0$ in [figure 7\(c\)](#). The velocity profiles are qualitatively similar at $x/h_0 = 0$ in the Case 5 and Case 0 simulations with a thick viscous sublayer extending until $z^+ \approx 20$, a relatively thin log-law sublayer where $\kappa \approx 0.28$, and a thick constant velocity layer extending until the air–water interface. It is relevant to point out that the velocity profiles near the lock-gate have a similar behaviour in the non-Newtonian and Newtonian cases even though the dynamic molecular viscosity, μ , varies by more than one order of magnitude in between the channel bed and the air–water interface (e.g. see profile of μ/μ_w at $x/h_0 = 0$ in [figure 7\(e\)](#), where μ_w is the dynamic molecular viscosity at the channel bed) in Case 5.

The predicted profiles at $x/h_0 = 12.5$ when the front is situated at $x/x_f = 25$ in [figures 6](#) and [7](#) are used to illustrate differences between the structure of non-Newtonian and Newtonian dam-break waves in the regions where the wave flow is strongly turbulent. In both Case 0 and Case 5 simulations, the viscous sublayer extends until $z^+ \approx 5$. Though a well-developed log-law sublayer is present in both simulations, this layer starts at $z^+ \approx 80$ in Case 0 and at $z^+ \approx 100$ in Case 5. Also, the thickness of the log-law sublayer decays in the non-Newtonian case. For example, the interface with the constant velocity layer is situated around $z/z_{max} = 0.41$ ($z^+ \approx 850$) in Case 0 and $z/z_{max} = 0.32$ ($z^+ \approx 1000$) in Case 5. This effect is consistent with the observed behaviour of non-Newtonian shear-thinning fluids that are characterised by a flattened velocity profile due to the increase of the dynamic molecular viscosity away from the wall (e.g. see profile of μ/μ_w at $x/h_0 = 12.5$ in [figure 7e](#)).

While inside the regions of the dam-break wave generated in Case 0, where turbulence is strong the slope of the log law corresponds to $\kappa \approx 0.4$, the predicted value of κ is close to 0.26 in the non-Newtonian dam-break wave generated in Case 5 ([figure 7b](#)). This value is slightly lower than the value observed at $x/h_0 = 0$ in Case 5 ([figure 7a](#)).

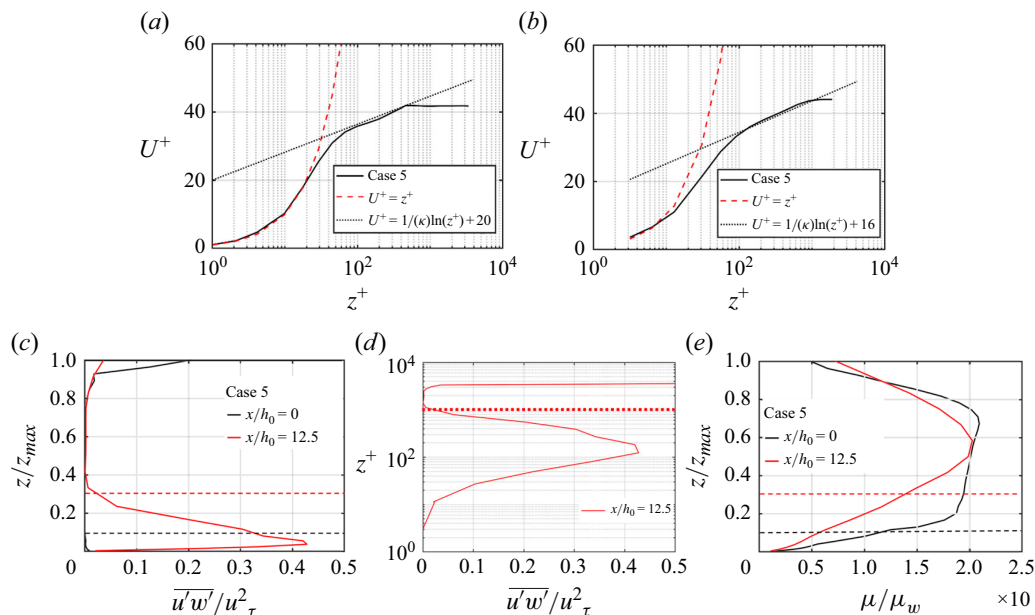


Figure 7. Vertical structure of the mean flow and primary turbulent shear stress, $\overline{u'w'}$, for Case 5. Results are shown when the front is situated at $x_f/h_0 = 25$. (a) Streamwise (spanwise-averaged) velocity profile at $x/h_0 = 0$ (lock gate), $\kappa = 0.28$; (b) streamwise (spanwise-averaged) velocity profile at $x/h_0 = 12.5$, $\kappa = 0.26$; (c) $\overline{u'w'}$ profile at $x/h_0 = 12.5$; (d) $\overline{u'w'}$ profile at $x/h_0 = 12.5$ in wall coordinates; (e) non-dimensional (spanwise-averaged) dynamic molecular viscosity profiles. The horizontal dotted lines in panels (c), (d) and (e) correspond to the boundary between the logarithmic layer and the constant velocity layer of the dam-break wave.

The fact that the slope of the log law (i.e. $1/\kappa$) in regions where the flow is strongly turbulent is significantly higher for non-Newtonian dam-break waves compared with the value observed for Newtonian waves is not surprising and is consistent with the behaviour observed for simpler steady turbulent flows. For example, values of κ close to 0.26 were reported for non-Newtonian fluids with a power law index $n = 0.5$ in steady turbulent pipe-flow experiments by Rudman *et al.* (2004) and in LES of the same type of flows by Gnambo *et al.* (2015).

In the region of strong turbulence inside the wave, the peak of $\overline{u'w'}$ is situated at approximately 100–200 wall units from the channel bed in Case 5 (figure 7d), which is comparable to the value (~ 100 wall units) predicted for the Newtonian dam-break wave in Case 0. Moreover, in both simulations, the primary shear stress decays monotonically inside the log-law sublayer and reaches its minimum slightly above the boundary between the log-law sublayer and the constant velocity layer. The values of $\overline{u'w'}$ are negligible inside the lower part of the constant velocity layer (figure 7d), which was not the case for the Newtonian dam-break wave (figure 6e). Though in both simulations, $\overline{u'w'}$ increases rapidly inside the top part of the constant velocity layer ($z/z_{max} > 0.8$), the rate of increase is lower for the non-Newtonian dam-break wave due to the weaker instabilities developing along the air–fluid interface in this case.

4. Dam-break wave dynamics

In addition to investigating the wave dynamics and, in particular, the temporal evolution of the front position during the different phases of the wave propagation, this section uses

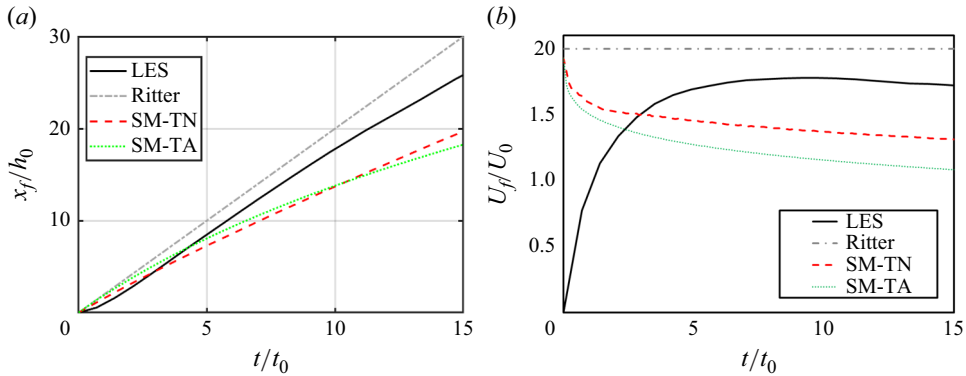


Figure 8. Temporal evolution of the (a) non-dimensional front position and (b) front velocity for Case 0. Results of the shallow-water turbulent numerical model (SM-TN) and analytical solutions (SM-TA, Ritter) are compared with LES predictions.

the 3-D LES as numerical experiments with respect to which the predictive abilities of simpler SWE numerical models (SM-LN and SM-TN, see § 2.3.2) and analytical solutions (SM-TA, Ritter, Hogg & Pritchard, see § 2.3.3) are assessed.

4.1. Newtonian dam-break waves

Case 0 is used to illustrate the temporal evolution of the front position, the wave shape and the bed shear stress characteristics in turbulent dam-break waves of Newtonian fluids. It also serves as a limiting case to discuss dam-break waves of non-Newtonian fluids. The performance of turbulent SWE analytical (SM-TA) and numerical (SM-TN) models is discussed. For the sake of completeness, the comparison with the Ritter solution is also included.

Figure 8(a) compares the temporal evolution of the front position predicted by LES with those given by the SM-TA and SM-TN models and Ritter's solution for Case 0. LES results show two distinct phases. During the initial acceleration phase, when the fluid inside the wave increases its velocity by releasing potential energy, the turbulence and viscous dissipation are negligible. The accelerating phase is followed by a deceleration phase, starting at approximately $t/t_0 = 8$ (figure 8b), during which bed friction effects are important. In contrast, the SW-TA and SW-TN models predict that the deceleration phase starts very soon after the release of the lock. This happens because the bottom turbulent shear stress is applied starting at $t/t_0 = 0$.

During the deceleration phase, the temporal evolution of the front position predicted by LES can be described by a power-law relationship $x_f/h_0 = \gamma(t/t_0)^\alpha$. Since in practical applications one is generally interested in characterising the dam-break evolution at large times after the gate opening, the predictive capabilities of the shallow models are mainly assessed based on how well they can predict the values of α and γ inferred from LES (i.e. $\alpha = 0.885$ and $\gamma = 2.38$). The SWE analytical and numerical models predict fairly close values of the power-law exponent ($0.8 < \alpha < 0.87$, see table 3).

Another important requirement for SWE numerical simulations is to accurately predict the sediment entrainment capacity in applications where the dam-break wave propagates over an erodible bed. Figure 9 compares the distributions of the non-dimensional bed shear stress predicted by LES and the SM-TN model in between the lock gate and the front when $x_f = 25h_0$. LES predicts a close to linear decay of the bed shear stress from the lock gate until close to the front, with local variations due to the resolved turbulent eddies inside

CASE	k [(Pa s) n]	n [–]	Re_{MR}	α (LES)	α (LES)	α (SM- LN)	γ (SM- LN)	α (SM- TN)	γ (SM- TN)	α (SM- TA)	γ (SM- TA)	α (HM- LA)	γ (HM- LA)
0	9.00×10^{-4}	1	2.18×10^5	0.885	2.38	—	—	0.870	1.80	0.801	2.52	—	—
1	9.00×10^{-2}	0.9	4.12×10^3	0.830	1.94	0.797	2.32	0.850	1.74	0.861	1.65	0.85	2.08
2	9.00×10^{-2}	0.6	2.15×10^4	0.886	2.01	0.784	3.31	0.867	1.82	0.865	1.73	0.82	2.98
3	9.00×10^{-2}	0.3	1.26×10^5	0.916	2.31	0.782	4.73	0.885	1.94	0.866	1.85	0.79	4.5
4	9.00×10^{-2}	0.1	5.70×10^5	0.968	2.05	0.820	4.64	0.903	1.98	0.867	1.91	0.82	4.66
5	9.00×10^{-3}	0.6	2.73×10^5	0.892	1.98	0.815	4.56	0.882	1.89	0.876	1.82	0.82	4.52
6	9.00×10^{-4}	0.6	2.97×10^6	0.957	2.08	0.825	6.67	0.902	1.92	0.890	1.86	0.82	6.86

Table 3. Power-law coefficients predicted by the different simulations and analytical solutions during the deceleration phase. Values predicted by the Hogg & Pritchard (2004) solution (HM-LA) are also reported. Re_{MR} is the spanwise- and streamwise-averaged Metzner Reynolds number (Dodge & Metzner 1959) calculated when $x_f/h_0 = 25$.

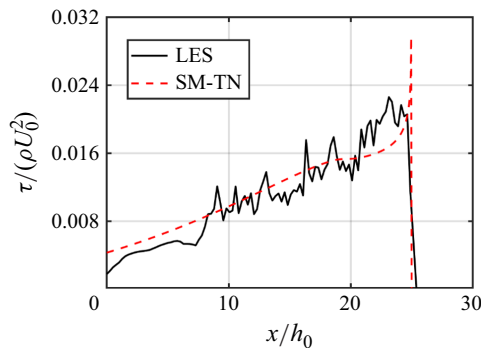


Figure 9. Non-dimensional (spanwise-averaged) bed shear stress distribution for Case 0. The model predictions of the shallow-water turbulent numerical model (SM-TN) are compared with LES predictions when $x_f/h_0 = 25$.

the wave. Except for the larger amplification of the bed shear stress very close to the front, the use of a turbulent-flow friction coefficient leads to very close agreement of the SM-TN model with LES.

Given that the passage of a dam-break wave can induce severe flooding, it is important to also discuss how well SWE models predict the free surface profile. In addition to the SM-TN and SM-TA profiles, figure 10 also includes Ritter’s solution. Consistent with figure 8, the front in Ritter’s solution has travelled a considerably larger distance compared with the wave predicted by LES. However, the water depth in Ritter’s solution is very small in between $x/h_0 \approx 19$ and the front so, overall, Ritter’s solution provides a good approximation to the free surface profile predicted by LES. Although the propagation length of the wave is underpredicted in the SM-TN simulation, the flow depth is reproduced quite accurately until the front region. Qualitatively, the analytical model SM-TA shows a similar behaviour, though it slightly overestimates the flow depth over part of the wave body compared with SM-TN. Overall, the use of a friction formula based on turbulent flows results in fairly accurate predictions of the water–air interface and bed shear stress distributions beneath the deeper parts of the wave.

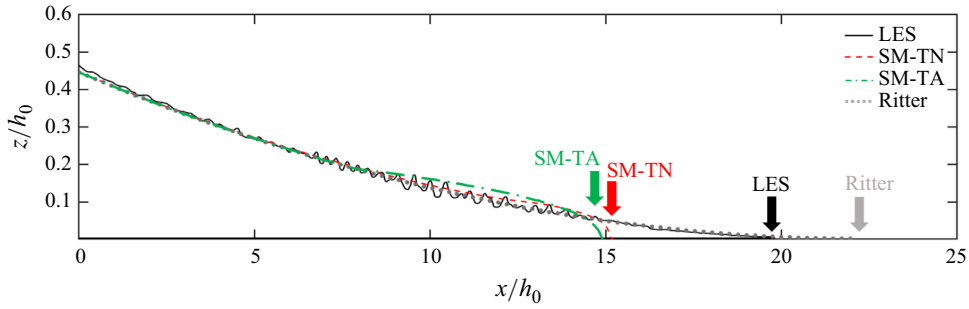


Figure 10. Top (free surface) boundary of the dam break wave for Case 0. LES predictions are compared with the shallow-water turbulent numerical model (SM-TN) and analytical solutions (SM-TA, Ritter) at $t/t_0 = 11.2$. The vertical arrows show the position of the front predicted by the different models.

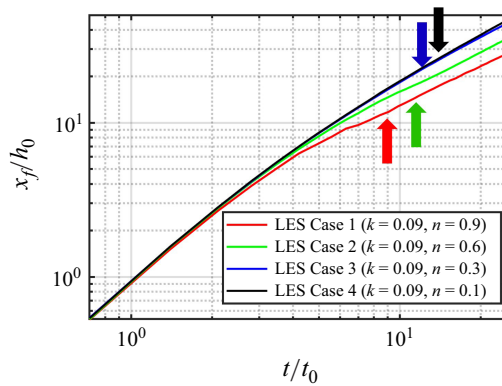


Figure 11. Effect of the power law index, n , on the temporal evolution of the non-dimensional front position. Vertical arrows show the onset of the deceleration phase.

4.2. Non-Newtonian dam-break waves: power-law index effect

As shown in figure 11, the temporal evolution of the non-dimensional front position in the LES (Case 1 to Case 4) conducted with a constant value of the consistency index ($k = 0.09$) is strongly influenced by n . Lower values of n , corresponding to a stronger shear-thinning behaviour of the fluid, result in a faster wave propagation after the end of the acceleration phase. These findings are consistent with the theoretical understanding of non-Newtonian rheology, where shear-thinning fluids experience reduced resistance under high-shear conditions. In particular, near the front, where strong shear is generated inside the wave, a faster propagation of the front with decreasing n is observed in the simulations. LES results show that the temporal evolution of the front position during the deceleration phase is well described by the power-law relationship discussed for waves of Newtonian fluids and that α increases monotonically with decreasing n (table 3). Moreover, for very small values of n , the power law exponent approaches a value of one ($\alpha = 0.968$ for $n = 0.1$). Varying n while keeping the consistency index constant has only a small effect on the value of the power-law parameter, γ (table 3).

In the following discussion, results of the SM-LN and SM-LA are included to highlight the inconsistencies that may arise from neglecting the presence of turbulence in SWE models. The use of a laminar friction coefficient in the SM-LN simulation leads to an increased velocity of the front compared with LES, while the opposite is observed for

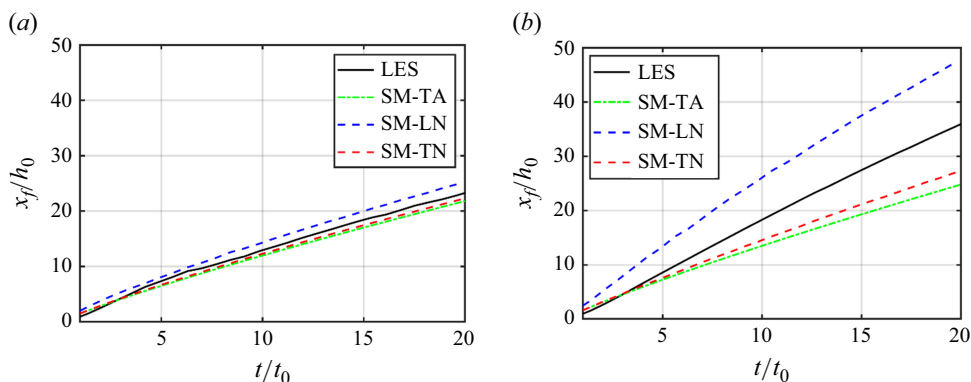


Figure 12. Temporal evolution of the non-dimensional front position predicted by LES, the shallow-water laminar (SM-LN) and turbulent (SM-TN) numerical models, and by the analytical solution (SM-TA). (a) Case 1; (b) Case 3.

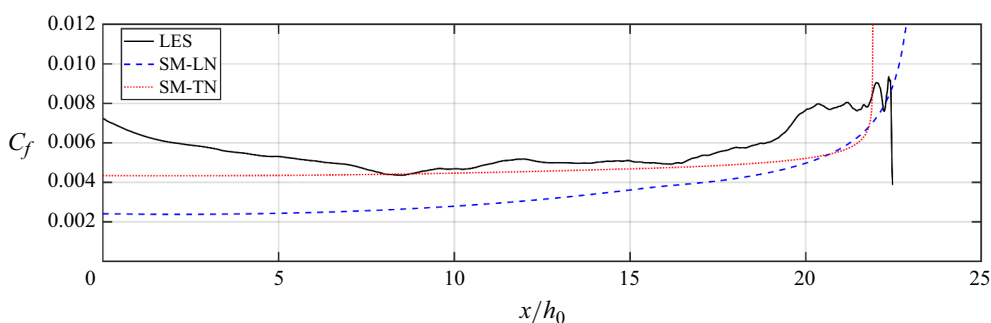


Figure 13. Friction coefficient distribution for Case 1. The LES predictions are compared with those of the SM-LN and SM-TN numerical models when $x_f/h_0 = 22.5$.

the SM-TN simulation using a turbulent friction coefficient (see results in [figure 12](#) for Case 1 and Case 3). The predictions of the SM-TA solution using the turbulent friction coefficient are close to those given by the corresponding SM-TN numerical model. For all non-Newtonian dam-break cases, SM-TA is slightly more dissipative than SM-TN, which explains the faster propagation of the front predicted by SM-TN in [figure 12\(b\)](#).

The implementation of the friction coefficient formula (2.14) for turbulent condition significantly improves the accuracy of the SWE model in predicting the propagation of the front especially for lower values of n . For example, results for Case 3 ($n = 0.3$) in [figure 12\(b\)](#) show that compared with LES, the overprediction of the front position by SM-LN is approximately 50 % larger than the underprediction of the front position by SM-TN. For higher values of n like Case 1 ($n = 0.9$) in [figure 12\(a\)](#), SWE model predictions are in good agreement with LES for both types of friction coefficients, with SM-TN and SM-TA showing slightly better agreement with LES than SM-LN.

The better performance of the SM-TN model to predict the front propagation is primarily due to ability of the Dodge and Metzner formula to more accurately capture the distribution of the friction coefficient beneath the turbulent dam break wave, as illustrated in [figure 13](#) for Case 1 ($n = 0.9$). Conversely, the SM-LN model underestimates the resistance.

For non-Newtonian fluid cases, the relative performance of the SWE models with respect to LES in predicting the free surface profile and the depth levels inside the wave is similar to that observed for Newtonian fluid cases ([figure 10](#)). For example, the SM-TN

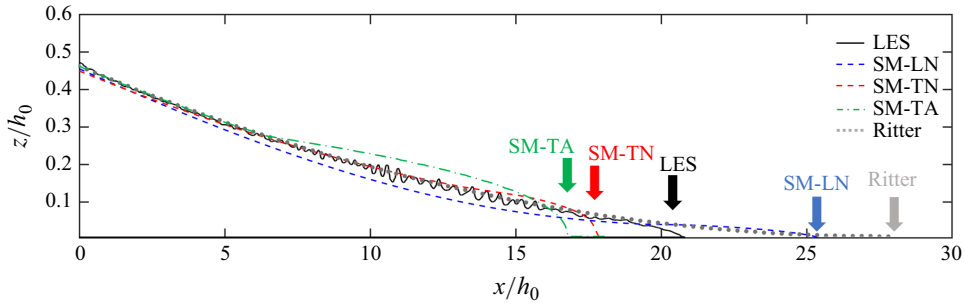


Figure 14. Top (free surface) boundary of the dam break-wave for Case 2 shown at $t/t_0 = 14$. The vertical arrows show the front position predicted by LES and the different SWE models.

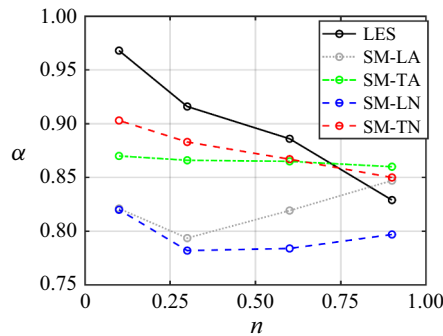


Figure 15. Power-law coefficient during the deceleration phase as a function of the power law index, n , for the different models.

model gives the closest predictions of the depth levels inside the wave generated in Case 2 compared with LES (figure 14). The SM-LN model underestimates the wave depth over an important fraction of the wave's length. Meanwhile, the SM-TA model overestimates the wave depth. Ritter's solution significantly overestimates the propagation distance of the front. This is fully expected, given that there is no deceleration phase in Ritter's solution ($\alpha = 1$). However, it is interesting that the wave-depth levels predicted by Ritter's solution away from the front region provide a good approximation to LES predictions, better than that shown by the SM-LN model.

The power-law relationship $x_f/h_0 = \gamma(t/t_0)^\alpha$ that provides a good approximation of the front evolution during the deceleration phase in the LES performed with non-Newtonian fluids can also be used to approximate the front evolution predicted by the SWE models. Figure 15 summarises the variation of α with n obtained using LES, SWE numerical models, and the analytical outputs of the model proposed in this work (SM-TA) and that of Hogg & Pritchard (2004) for laminar dam-break flows (HM-LA).

SWE models that assume a turbulent friction coefficient (SM-TA and SM-TN) show a monotonically decreasing α with increasing n , as also predicted by LES. The main difference is the rate of decrease, with the SM-TA model showing the smallest rate of change of α with n . The largest differences in the predicted α values by the three models are observed for low values of n . This is explained by the inability of SWE models to predict the correct value of the friction coefficient in very shear-thinning fluids. Both models that assume laminar condition, SM-LN and HM-LA, predict that α decreases with n for low values of the power law index, while for $n > 0.3$, an increase is observed.

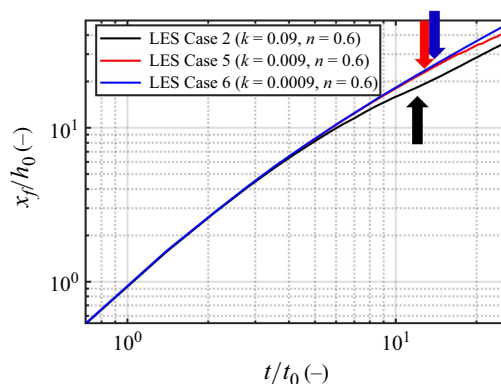


Figure 16. Effect of the consistency index, k , on the evolution of the non-dimensional front position. Vertical arrows show the onset of the deceleration phase.

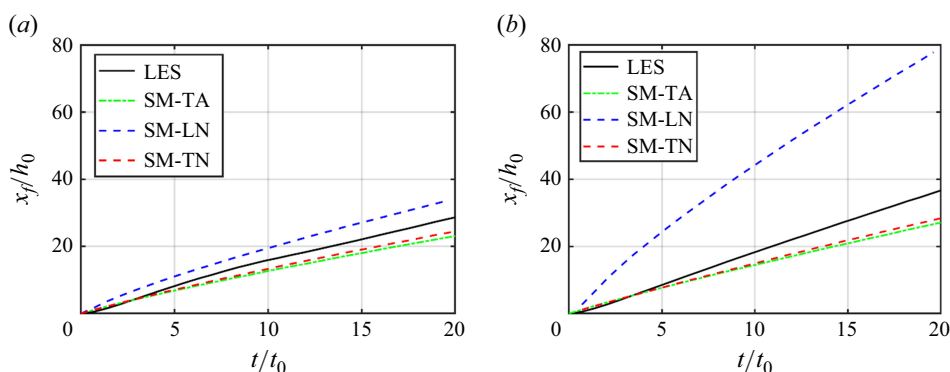


Figure 17. Temporal evolution of the non-dimensional front position predicted by LES and some of the SWE numerical models and analytical solutions. (a) Case 2; (b) Case 6.

4.3. Non-Newtonian dam-break waves: consistency index effect

The consistency index, k , characterises the fluid's resistance to deformation. Lower values of k indicate reduced molecular viscosity and an increased contribution of inertia in non-Newtonian fluid flows. Figure 16 compares the front propagation in LES conducted with $n = 0.6$. Compared with Case 2, the value of k was 10 times smaller in Case 5 and 100 times smaller in Case 6, resulting in higher Reynolds numbers (table 1). As shown in figure 16, the main effect of decreasing k is an acceleration of the front after the end of the acceleration phase once inertia effects dominate inside the body of the turbulent wave. The highest value of α ($= 0.957$) is observed for the highest Reynolds number simulation (Case 6, see table 3). This suggests that in the limit of a very small k , or infinite Reynolds number, α will approach one, which is consistent with Ritter's inviscid solution.

As observed in §4.2, the use of a laminar friction coefficient results in a faster propagation of the front compared with LES, while the opposite is true for SWE models using a turbulent friction coefficient. For both Case 2 and Case 6, the SM-LN model consistently shows larger differences with LES compared with those shown by the SM-TN model (figure 17). Moreover, the predictions of the analytical model using a friction coefficient based on (2.14) are very close to those obtained using a full SWE numerical model, as can be seen from comparing SM-TA and SM-TN predictions in figure 17.

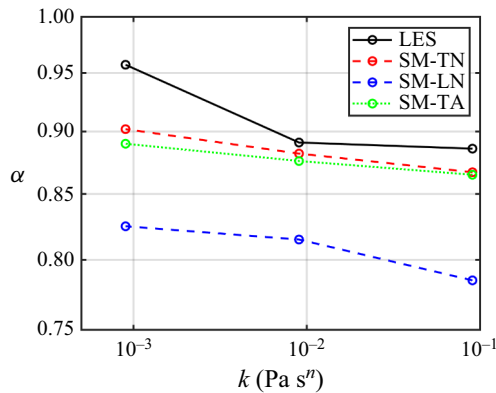


Figure 18. Power-law coefficient during the deceleration phase as a function of the consistency index, k , for the different models.

An important finding is that for a constant n , the absolute difference between the predictions of the numerical and analytical SWE models and those of LES is increasing with increasing Reynolds number (i.e. with decreasing k), as can be seen by comparing results for Case 2 and Case 6 in figures 17(a) and 17(b), respectively.

Similar to LES, all SWE models predict a monotonic decrease of α with increasing k , as shown in figure 18. The largest differences with LES are shown by the SM-LN model while, as indicated in table 3, the effect of k on α is negligible for the HM-LA solution ($\alpha \approx 0.82$ for the cases with $n = 0.6$). Except for very high Reynolds numbers, the α_2 values predicted by the numerical and analytical SWE models using a turbulent friction coefficient are very close (i.e. less than 3 % difference) to the value obtained from LES. For both SM-TN and SM-TA, the difference increases to 6 %–7 % for $k = 0.0009 \text{ (Pa s)}^{0.6}$. This value is significantly lower than the difference of approximately 14 % observed between the α values predicted by LES and the SM-LN model for $k = 0.0009 \text{ (Pa s)}^{0.6}$.

5. Summary and conclusions

The present study based on fully three-dimensional LES conducted at moderate and high Reynolds numbers showed that turbulence affects both the structure, and the propagation of Newtonian and non-Newtonian dam-break waves over a long horizontal surface. As direct numerical simulations of high-Reynolds-number dam-break waves are computationally too expensive, the use of 3-D LES using a dynamic model that can recognise regions where the flow is non-turbulent was critical to capture the correct flow physics. This is because the front part of such dam-break waves is strongly turbulent, while turbulence effects are generally small at large distances behind the front. Based on the 3-D simulation results, the paper reports several new main findings related to the structure and temporal evolution of turbulent dam-break waves over a horizontal smooth surface.

A first finding is that such waves are characterised by a two-layer structure. The vertical profiles of the spanwise-averaged streamwise velocity revealed the presence of a boundary-layer like region near the bed surface containing a log-law sublayer and of a constant velocity layer on top of it that extends until the fluid–air interface (i.e. the free surface). A second set of findings concerns the values of the von Kármán constant in the law of the wall and the variation of the primary shear stress. This information can be used in simpler

SWE numerical and theoretical approaches used to model the spatio-temporal evolution of dam break waves and to estimate quantities of engineering interest.

For Newtonian dam-break waves, the von Kármán constant was found to vary along the wave. More precisely, the standard value of 0.4 associated with turbulent boundary layers of Newtonian fluids was found to fit the velocity profiles only in the strongly turbulent regions situated near the front of the wave. However, its value decayed to approximately 0.28 in regions situated far from the front where turbulence effects were weak. Inside the strongly turbulent regions, the primary Reynolds shear stress peaked inside the boundary layer at approximately 100 wall units from the bed surface before reaching negligible values at the interface with the constant velocity layer. It then started increasing again inside the constant velocity layer.

In the case of turbulent dam-break waves of power-law fluids, the slope of the log law was found to vary less along the body of the wave. The von Kármán constant values ($\kappa = 0.26\text{--}0.28$) were close to previously reported values for steady turbulent flows of power-law fluids (e.g. pipe flows). Present results suggest that the reduction of κ inside the log-law sublayer is a general characteristic of turbulent flows involving non-Newtonian fluids. The behaviour of the primary Reynolds shear stress inside the boundary layer was qualitatively similar to that observed for waves of Newtonian fluids. Meanwhile, the values of the Reynolds shear stress remained very low inside most of the constant velocity layer in the high-Reynolds-number simulations conducted with a power-law fluid. The values of the Reynolds shear stress near the fluid–air interface were much smaller in the simulations performed with a non-Newtonian fluid, consistent with the weaker instabilities developing along the fluid–air interface compared with dam-break waves of Newtonian fluids. Another noticeable effect was the increase of the thickness of the constant velocity layer with decreasing power-law index in shear-thinning fluids. This effect was linked to the increase of the dynamic molecular viscosity away from the wall which induces a flattened streamwise velocity profile.

The third fundamental finding relates to the temporal evolution of the front position during the deceleration phase which can be well described by a power-law relationship for both Newtonian and non-Newtonian dam-break waves propagating over a smooth horizontal surface. The effect of increasing the shear-thinning behaviour of the fluid was investigated by performing a series of simulations with decreasing power-law index, n , while keeping the consistency index, k , constant. The main effect of decreasing n was to increase the speed of the front. Most of the differences built during the deceleration phase were due to the monotonic increase of the power-law exponent during the deceleration phase, α , with decreasing n . For very small values of n , LES predicted $\alpha \approx 1$, which is consistent with the inviscid flow limit when the front velocity remains constant. Decreasing k for constant n resulted in an acceleration of the front once inertia effects dominate inside the body of the wave (i.e. during the deceleration phase). The decrease of k is associated with an increase of the Reynolds number. LES predicted an increase of α with decreasing k . Based on the present results (i.e. $\alpha = 0.957$ for $k = 0.0009 \text{ (Pa s)}^{0.6}$), it is expected that α will approach one in the limit of an infinite Reynolds number, which is consistent with Ritter's inviscid solution.

Given that SWE-based models are widely used for engineering predictions of these flows (e.g. mudflows), it is important to have a clear idea of the accuracy of these models in predicting relevant quantities of interest used to evaluate the impact of the wave propagation on the environment and for hazard assessment. A main finding of the present study is that using a turbulent friction factor in SWE numerical models yields more accurate results for dam-break waves where at least the front part of the wave is turbulent.

As part of the present study, a novel 1-D SWE analytical model was proposed. The model employs a unitary value of the shape factor and a friction coefficient regression valid for a power-law fluid in the turbulent regime. The temporal evolution of the front predicted by the approximate analytical solution accounting for turbulent flow conditions was found to be in good agreement with that given by the corresponding SWE numerical model. In general, both the numerical and analytical solution of the newly proposed model show significantly better agreement with LES compared with the laminar SWE model. This is true not only for the temporal evolution of the wave front, but also for the bed shear stress distribution along the wave, which is an important quantity in applications where such waves propagate over an erodible bed. As such, this study shows that inclusion of turbulence effects in SWE theoretical models used to predict high-Reynolds-number non-Newtonian dam-break waves should increase the predictive capabilities of such models.

Acknowledgements. The authors would like to thank IIHR Hydrosience and Engineering for providing the computational resources to perform the simulations.

Competing interests. Authors declare that they have no competing interests.

Author contributions. A.D.G., G.C., A.V. conceptualisation; A.D.G., G.C., A.V., C.D.C. data curation; A.D.G., G.C., A.V., C.D.C. formal analysis; F.D.P. funding acquisition; A.D.G., A.V., C.D.C. investigation; G.C., A.V. methodology; F.D.P. project administration; G.C., A.V., C.D.C. software; A.D.G. validation; A.D.G. visualisation; A.D.G., G.C., A.V., C.D.C., F.D.P. original draft; A.D.G., G.C., A.V., C.D.C., F.D.P. review and editing.

REFERENCES

- ALEIXO, R., SOARES-FRAZÃO, S. & ZECH, Y. 2011 Velocity-field measurements in a dam-break flow using a PTV Voronoi imaging technique. *Exp. Fluids* **50**, 1633–1649.
- ALEIXO, R., ZECH, Y. & SOARES-FRAZÃO, S. 2014 Turbulence Measurements in Dam-Break Flows. In *Proceedings of the International Conference on Fluvial Hydraulics, River Flows 2012*, pp. 311–318. CRC Press.
- AURELI, F., MARANZONI, A., PETACCIA, G. & SOARES-FRAZÃO, S. 2023 Review of experimental investigations of dam-break flows over fixed bottom. *Water* **15** (6), 1229.
- BALMFORTH, N.J., CRASTER, R.V., PERONA, P., RUST, A.C. & SASSI, R. 2007 Viscoplastic dam breaks and the Bostwick consistometer. *J. Non-Newtonian Fluid Mech.* **142** (1–3), 63–78.
- BARTOSIK, A. 2010 Application of rheological models in prediction of turbulent slurry flow. *Flow Turbul. Combust.* **84**, 277–293.
- BASSO, F.O., FRANCO, A.T. & PITZ, D.B. 2022 Large-eddy simulation of turbulent pipe flow of Herschel–Bulkley fluids – assessing subgrid-scale models. *Comput. Fluids* **244**, 105522.
- BATES, P.D. 2022 Flood inundation prediction. *Annu. Rev. Fluid Mech.* **54** (1), 287–315.
- BENSLIMANE, A., BEKKOUR, K., FRANÇOIS, P. & BECHIR, H. 2016 Laminar and turbulent pipe flow of bentonite suspensions. *J. Petrol. Sci. Engng* **139**, 85–93.
- BLASIUS, H. 1913 ‘Das aehnlichkeitsgesetz bei reibungsvorgängen in flüssigkeiten’. In *Mitteilungen über Forschungsarbeiten Auf Dem Gebiete des Ingenieurwesens, Insbesondere der Technischen Hochschulen*. Springer.
- BLIGHT, G.E. 1997 Destructive mudflows as a consequence of tailings Dyke failures. *Proc. Inst. Civil Engrs Geotech. Engng* **125** (1), 9–18.
- BOGER, D.V. 2013 Rheology of slurries and environmental impacts in the mining industry. *Annu. Rev. Chem. Biomol.* **4**, 239–256.
- BURGER, J.H., HALDENWANG, R. & ALDERMAN, N.J. 2015 Laminar and turbulent flow of non-Newtonian fluids in open channels for different cross-sectional shapes. *J. Hydraul. Engng* **141** (4), 04014084.
- BURGER, J.H. 2014 Non-Newtonian open channel flow: the effect of shape. Doctoral dissertation, Cape Peninsula University of Technology, Cape Town, South Africa.
- CAMPOMAGGIORE, F., DI CRISTO, C., IERVOLINO, M. & VAGCA, A. 2016 Development of roll-waves in power-law fluids with non-uniform initial conditions. *J. Hydraul. Res.* **54** (3), 289–306.
- CAROTENUTO, C., MEROLA, M.C., ÁLVAREZ-ROMERO, M., COPPOLA, E. & MINALE, M. 2015 Rheology of natural slurries involved in a rapid mudflow with different soil organic carbon content. *Colloids Surf. A* **466**, 57–65.

- CASTRO-ORGAZ, O. & HAGER, W.H. 2019 Discussion of vertical 2D non-hydrostatic model using mode splitting for dam-break flows by Y. Zhu and D. Hu. *J. Hydraul. Engng* **145** (10), 07019007.
- CHANSON, H. 2009 Application of the method of characteristics to the dam break wave problem. *J. Hydraul. Res.* **47** (1), 41–49.
- CONSTANTINESCU, G. 2014 LE of shallow mixing interfaces: a review. *Environ. Fluid Mech.*, **14**, 971–996.
- DAI, A. & HUANG, Y. 2022 On the merging and splitting processes in the lobe-and-cleft structure at a gravity current head. *J. Fluid Mech.* **930**, A6.
- DEL GAUDIO, A., CONSTANTINESCU, G., DI CRISTO, C., DE PAOLA, F. & VACCA, A. 2024 Large eddy simulation of power-law fluid dam break wave impacting against a vertical wall. *Phys. Rev. Fluids* **9** (7), 074801.
- DELANNAY, R., VALANCE, A., MANGENEY, A., ROCHE, O. & RICHARD, P. 2017 Granular and particle-laden flows: from laboratory experiments to field observations. *J. Phys. D: Appl. Phys.* **50** (5), 053001.
- DENG, X., LIU, H. & LU, S. 2018 Analytical study of dam-break wave tip region. *J. Hydraul. Engng* **144** (5), 04018015.
- DODGE, D.W. & METZNER, A.B. 1959 Turbulent flow of non-Newtonian systems. *AIChE J.* **5** (2), 189–204.
- FRACCAROLLO, L. & TORO, E.F. 1995 Experimental and numerical assessment of the shallow water model for two-dimensional dam-break type problems. *J. Hydraul. Res.* **33** (6), 843–864.
- FERNÁNDEZ-NIETO, E.D., NOBLE, P. & VILA, J.P. 2010 Shallow water equations for non-Newtonian fluids. *J. Non-Newtonian Fluid Mech.* **165** (13–14), 712–732.
- GNAMBODE, P.S., ORLANDI, P., OULD-ROUISS, M. & NICOLAS, X. 2015 Large-eddy simulation of turbulent pipe flow of power-law fluids. *Intl J. Heat Fluid Flow* **54**, 196–210.
- GOTTLIEB, S. & SHU, C.-W. 1998 Total variation diminishing Runge-Kutta schemes. *Math. Comput.*, **67** (221), 73–85.
- HALDENWANG, R., KOTZÉ, R., SLATTER, P. & MARIETTE, O. 2006 An Investigation in Using UVP for Assisting in Rheological Characterization of Mineral Suspensions. In *Proceedings of the 5th International Symposium on Ultrasonic Doppler Methods for Fluid Mechanics and Fluid Engineering*, pp. 77–79.
- HARTEN, A., LAX, P.D. & VAN LEER, B. 1983 On upstream differencing and Godunov-type schemes for hyperbolic conservation laws. *SIAM Rev.* **25** (1), 35–61.
- HIRT, C.W. & NICHOLS, B.D. 1981 Volume of fluid (VOF) method for the dynamics of free boundaries. *J. Comput. Phys.* **39** (1), 201–225.
- HOGG, A.J. & PRITCHARD, D. 2004 The effects of hydraulic resistance on dam-break and other shallow inertial flows. *J. Fluid Mech.* **501**, 179–212.
- HORNA-MUNOZ, D. & CONSTANTINESCU, G. 2018 A fully 3D numerical model to predict flood wave propagation and assess efficiency of flood protection measures. *Adv. Water Resour.* **122**, 148–165.
- HORNA-MUNOZ, D. & CONSTANTINESCU, G. 2020 3D dam break flow simulations in simplified and complex domains. *Adv. Water Resour.* **137**, 103510.
- HUANG, X. & GARCIA, M.H. 1998 A Herschel–Bulkley model for mud flow down a slope. *J. Fluid Mech.* **374**, 305–333.
- KARAHAN, D.T., RANJAN, D. & AIDUN, C.K. 2023 Turbulent channel flow of generalized newtonian fluids at $Re = 180$. *J. Non-Newtonian Fluid Mech.*, **314**, 105015.
- LAROCQUE, L.A., IMRAN, J. & CHAUDHRY, M.H. 2013a Experimental and numerical investigations of two-dimensional dam-break flows. *J. Hydraul. Engng* **139** (6), 569–579.
- LAROCQUE, L.A., IMRAN, J. & CHAUDHRY, M.H. 2013b 3D numerical simulation of partial breach dam-break flow using the LES and $k-\epsilon$ turbulence models. *J. Hydraul. Res.* **51** (2), 145–157.
- LEVEQUE, R.J., GEORGE, D.L. & BERGER, M.J. 2011 Tsunami modelling with adaptively refined finite volume methods. *Acta Numer.* **20**, 211–289.
- LIU, K.F. & MEI, C.C. 1989 Slow spreading of a sheet of Bingham fluid on an inclined plane. *J. Fluid Mech.* **207**, 505–529.
- LIU, Y., BALMFORTH, N.J., HORMOZI, S. & HEWITT, D.R. 2016 Two-Dimensional viscoplastic dambreaks. *J. Non-Newtonian Fluid Mech.* **238**, 65–79.
- MARANZONI, A. & TOMIROTTI, M. 2023 Three-dimensional numerical modelling of real-field dam-break flows: review and recent advances. *Water* **15** (17), 3130.
- MINUSSI, R.B. & MACIEL, G.F. 2012 Numerical experimental comparison of dam break flows with non-Newtonian fluids. *J. Brazil Soc. Mech. Sci. Engng* **34**, 167–178.
- MITISHITA, R.S., MACKENZIE, J.A., ELFRING, G.J. & FRIGAARD, I.A. 2021 Fully turbulent flows of viscoplastic fluids in a rectangular duct. *J. Non-Newtonian Fluid Mech.* **293**, 104570.
- MISHRA, P. & TRIPATHI, G. 1971 Transition from laminar to turbulent flow of purely viscous non-newtonian fluids in tubes. *Chem. Engng Sci.* **26**, 915–921.

- MUCHIRI, D.K., HEWETT, J.N., SELLIER, M., MOYERS-GONZALEZ, M. & MONNIER, J. 2024 Numerical simulations of dam-break flows of viscoplastic fluids via shallow water equations. *Theor. Comput. Fluid Dyn.* **38** (4), 557–581.
- NG, C.O. & MEI, C.C. 1994 Roll waves on a shallow layer of mud modelled as a power-law fluid. *J. Fluid Mech.* **263**, 151–184.
- NYCANDER, J., HOGG, A.M.C. & FRANKCOMBE, L.M. 2008 Open boundary conditions for nonlinear channel flow. *Ocean Model.* **24** (3–4), 108–121.
- OOI, S.K., CONSTANTINESCU, G. & WEBER, L. 2009 Numerical simulations of lock-exchange compositional gravity current. *J. Fluid Mech.* **635**, 361–388.
- PIRULLI, M., BARBERO, M., MARCHELLI, M. & SCAVIA, C. 2017 The failure of the stava valley tailings dams (Northern Italy): numerical analysis of the flow dynamics and rheological properties. *Geoenviron. Disasters* **4**, 1–15.
- PIERSON, T.C. 2005 Hyperconcentrated flow — transitional process between water flow and debris flow. In *Debris-Flow Hazards and Related Phenomena*. Springer Praxis Books. Springer.
- RITTER, A. 1892 Die fortpflanzung der wasserwellen. *Z. Ver. Dtsch. Ing.* **36** (33), 947–954.
- RODI, W., CONSTANTINESCU, G. & STOEßER, T. 2013 Large-eddy simulation in hydraulics, CRC Press, Taylor & Francis Group., ISBN-10: 1138000247.
- RUDMAN, M., BLACKBURN, H.M., GRAHAM, L.J.W. & PULLUM, L. 2004 Turbulent pipe flow of shear-thinning fluids. *J. Non-Newtonian Fluid Mech.* **118**, 33–48.
- SCHAEER, N., VAZQUEZ, J., DUFRESNE, M., ISENMAN, G. & WERTEL, J. 2018 On the determination of the yield surface within the flow of yield stress fluids using computational fluid dynamics. *J. Appl. Fluid Mech.* **11** (4), 971–982.
- SHAO, S. & LO, E.Y.M. 2003 Incompressible SPH method for simulating newtonian and non-newtonian flows with a free surface. *Adv. Water Resour.* **26**, 787–800.
- SIMSEK, O. & ISLEK, H. 2023 2D and 3D numerical simulations of dam-break flow problem with RANS, DES, and LES. *Ocean Engng* **276**, 114298.
- SINGH, J., RUDMAN, M., BLACKBURN, H.M., CHRYSS, A., PULLUM, L. & GRAHAM, L.J.W. 2016 The importance of rheology characterization in predicting turbulent pipe flow of generalized newtonian fluids. *J. Non-Newtonian Fluid Mech.* **232**, 11–21.
- TAKAHASHI, T., Taylor, FRANCIS, BALKEMA, LEIDEN.TENG, J., JAKEMAN, A.J., VAZE, J., CROKE, B.F.W., DUTTA, D. & KIM, S.J.E.M. 2014 Debris flows: mechanics, prediction and countermeasures, flood inundation modelling: a review of methods, recent advances and uncertainty analysis. *Environ. Modell. Softw.* **90**, 201–216, 2017.
- TOKYAY, T. & CONSTANTINESCU, G. 2015 The effects of a submerged non-erodible triangular obstacle on bottom propagating gravity currents. *Phys. Fluids* **27** (5), 056601.
- TOKYAY, T., CONSTANTINESCU, G. & MEIBURG, E. 2012 Tail structure and bed friction velocity distribution of gravity currents propagating over an array of obstacles. *J. Fluid Mech.* **694**, 252–291.
- VALETTE, R., PEREIRA, A., RIBER, S., SARDO, L., LARCHER, A. & HACHEM, E. 2021 Visco-plastic dam-breaks. *J. Non-Newtonian Fluid Mech.* **287**, 104447.
- VISINTAINER, R., MATOUŠEK, V., PULLUM, L. & SELLGREN, A. 2023 Non-newtonian slurries and suspensions. In *Slurry Transport Using Centrifugal Pumps*, pp. 159–207. Springer International Publishing.
- WHITHAM, G.B. 1955 The Effects of Hydraulic Resistance in the Dam-Break Problem. *Proc. R. Soc. Lond. A. Math. Phys. Sci.* 399–407, 1170).
- WÜTHRICH, D., PFISTER, M., NISTOR, I. & SCHLEISS, A.J. 2018 Experimental study of tsunami-like waves generated with a vertical release technique on dry and wet beds. *J. Waterway Port Coastal Ocean Engng* **144** (4), 04018006.
- ZHANG, X., BAI, Y. & NG, C.O. 2010 Rheological properties of some marine muds dredged from china coasts. In *Proceedings of the 28 International Offshore and Polar Engineering Conference*, pp. 455–461.